2016-07-11

A residual-based shock capturing scheme for the continuous/discontinuous spectral element solution of the 2D shallow water equations

Marras, Simone; Kopera, Michal A.; Constantinescu, Emil M.; Suckale, Jenny; Giraldo, Francis X.

None found
http://hdl.handle.net/10945/55667

A Residual-based Shock Capturing Scheme for the Continuous/Discontinuous Spectral Element Solution of the 2D Shallow Water Equations

Simone Marras[a,*], Michal A. Kopera[b], Emil M. Constantinescu[c,d], Jenny Suckale[a], Francis X. Giraldo[e]

[a]*Stanford University, Dept. of Geophysics, Stanford, CA. U.S.A.*
[b]*University of California, Santa Cruz, CA, U.S.A.*
[c]*Argonne National Laboratory, Mathematics and Computer Science, Argonne, IL, U.S.A.*
[d]*The University of Chicago, Computation Institute, Chicago, IL, U.S.A.*
[e]*Naval Postgraduate School, Dept. of Applied Mathematics, Monterey, CA, U.S.A.*

Abstract

The high-order numerical solution of the non-linear shallow water equations is susceptible to Gibbs oscillations in the proximity of strong gradients. In this paper, we tackle this issue by presenting a shock capturing model based on the numerical residual of the solution. Via numerical tests, we demonstrate that the model removes the spurious oscillations in the proximity of strong wave fronts while preserving their strength. Furthermore, for coarse grids, it prevents energy from building up at small wave-numbers. The model has no tunable parameter and, if applied to the continuity equation to stabilize the water surface, the addition of the shock capturing scheme does not affect mass conservation. We found that our model improves the continuous and discontinuous Galerkin solutions alike in the proximity of sharp fronts propagating on wet surfaces. In the presence of wet/dry interfaces, however, the model needs to be enhanced with the addition of an inundation scheme. In this paper, we simply rely on the presence of a relatively small layer of water in the regions that should be dry.

*Corresponding author
Email address: smarras@stanford.edu (Simone Marras)

1. Introduction

The shallow water equations (SW) [16] are a common $(d-1)$ approximation to the d–dimensional Navier-Stokes equations to model incompressible, free surface flows. Due to the ability of high-order Galerkin methods to keep dissipation and dispersion errors low [5] and their flexibility with arbitrary geometries and *hp*-adaptivity, these methods are proving their mettle for solving the shallow water equations in the modeling of non-linear waves in different geophysical flows [46, 33, 59, 23, 24, 15, 42, 51, 26, 65, 34, 18, 37, 38, 47, 62, 22, 31, 32, 44, 14]. One important property that high-order Galerkin methods offer and that makes them attractive over their low-order counterparts is given by their natural strong scaling properties on massively parallel computers [50, 3, 20]. Nevertheless, the high-order solution of non-linear wave problems via high-order methods is susceptible to unphysical Gibbs oscillations that form in the proximity of strong gradients such as propagating bores. Filters such as Vandeven's and Boyd's [63, 9] and different types of artificial viscosities are the most common tools to handle this problem for continuous and discontinuous Galerkin (CG/DG). However, filtering may not be sufficient as the flow strengthens and the wave sharpness intensifies; for this reason, previous studies have stabilized the Galerkin solution to the shallow water equations in a variety of ways. For example, the Lilly-Smagorinsky eddy viscosity model [45, 56] was utilized in [54] and [55] to preserve numerical stability without compromising the overall quality of the solution. To account for sub-grid scale effects, artificial viscosity was utilized in the DG model described in [28] to improve their inviscid simulations. Recently, in [53] the high-order spectral element solution of the one-dimensional shallow water equations was stabilized via the entropy viscosity method. Artificial viscosity, limiters, and filters for the (modal) DG solution of SW were recently compared in [49], concluding that a dynamically adaptive viscosity may be the most effective means of regularization at higher orders.

Building on some of the insights from the authors above and on the findings of some authors of this paper to solve non-linear hyperbolic equations in the context of atmospheric modeling [48, §5], we propose a parameter-free shock capturing scheme to detect the presence of spurious modes in the proximity of strong gradients. The model that we propose –we will often refer to it as $Dyn-SGS$ to indicate its *dynamic* $sub-grid$ *scale* nature– was first defined in [52] for the linear finite element solution of compressible flows with shock waves. It was recently applied to stabilize high-order Galerkin methods in the context of stratified, low Mach number atmospheric flows by some of the authors in [48]. Similar to large eddy simulation (LES), $Dyn-SGS$ is based on the idea of scale splitting, where the flow scales are split into resolvable and unresolvable for a given computational grid. The unresolved scales are parameterized via the subgrid scale (SGS) model at hand ($Dyn-SGS$, in this case). It must be borne in mind throughout the manuscript that $Dyn-SGS$, unlike the sub-grid scale models designed for LES that are built from physical reasoning, is merely a numerical tool meant to remove the spurious oscillations from the solution of nonlinear wave equations and does not have, a priori, a physical meaning. Among its characteristics, being parameter-free and dynamically adaptive as a function of the solution residuals are possibly the most attractive ones. Furthermore, this model is independent of the underlying numerical approximation, which makes it naturally applicable to CG and DG alike, as well as to finite elements, finite volumes, and finite differences.

2. Governing equations

Let $\Omega \in \mathbb{R}^d$ be a fixed domain of space dimension d with boundary Γ and Cartesian coordinates $\mathbf{x} = [x]$ in 1D and $\mathbf{x} = [x, y]$ in 2D; in both cases, we will use z to identify the direction of gravity which is orthogonal to $\mathbf{x}$ and points downward. Let $t \in \mathbb{R}^+$ identify time. Given Ω and t we define the velocity vector $\mathbf{u}(t,\mathbf{x})$ whose one- and two-dimensional components are, respectively, $[u]$ and $[u,v]$. We also define the total water surface $H(t,\mathbf{x}) = H_s(t,\mathbf{x}) + H_b(\mathbf{x})$, where $H_s(t,\mathbf{x})$ is the water depth and $H_b(\mathbf{x})$ the bathymetry. Based on these definitions, the shallow water equations with artificial viscosity are written as:

$$\frac{\partial H}{\partial t} + \nabla \cdot (H\mathbf{u}) = \delta \nabla \cdot (\mu_{SGS} \nabla H), \tag{1a}$$

$$\frac{\partial H\mathbf{u}}{\partial t} + \nabla \cdot \left(H\mathbf{u} \otimes \mathbf{u} + \frac{g}{2}(H^2 - H_b^2)\mathbf{I} \right) + gH_s \nabla \cdot (H_b \mathbf{I}) = \nabla \cdot (H_s \mu_{SGS} \nabla \mathbf{u}), \tag{1b}$$

where $g = 9.81\,\mathrm{m\,s^{-2}}$ is the magnitude of the acceleration of gravity, $\mathbf{I}$ is the $d \times d$ identity matrix, and μ_{SGS} is the dynamic viscosity coefficient to be defined shortly. In (1a), the δ coefficient defines whether viscosity is turned on ($\delta = 1$) or off ($\delta = 0$) in the continuity equation. The shallow water equations above contain no physical viscosity or a Chézy-Manning formulation. We do this on purpose because we are interested in evaluating the net effect of $Dyn-SGS$ on the numerical solution without being affected by the presence of physical dissipation.

3. Space and time discretization

The numerical model used in this paper is the two-dimensional version of the NUMA model described in [24] and [4], where the equations are approximated via high-order continuous and discontinuous spectral elements on quadrilateral elements. Throughout the paper we will use the acronyms SEM or CG for spectral element/continuous Galerkin and DG for discontinuous Galerkin. The solution is advanced in time using a fully implicit Runge-Kutta scheme (see §3.2).

3.1. Spectral element and discontinuous Galerkin approximations

We point the reader to [24, 40] for details of the discretization; nonetheless, we introduce the notation that we adopt in this paper. To solve the shallow water equations by element-based Galerkin methods on a domain Ω, we proceed by defining the weak form of (1) that we first recast in compact notation as

$$\frac{\partial \mathbf{q}}{\partial t} + \nabla \cdot \mathbf{F}(\mathbf{q}) = \mathbf{S}(\mathbf{q}), \tag{2}$$

where $\mathbf{q} = [H, H\mathbf{u}]^{\mathrm{T}}$ is the transposed array of the solution variables and $\mathbf{F}$ and $\mathbf{S}$ are the flux and source terms.

In the case of spectral elements, the space discretization yields the semi-discrete matrix problem

$$\frac{\partial \mathbf{q}}{\partial t} = \widehat{\mathbf{D}}^{\mathrm{T}} \mathbf{F}(\mathbf{q}) + \mathbf{S}(\mathbf{q}) \tag{3}$$

where, for the global mass and differentiation matrices, $\mathbf{M}$ and $\mathbf{D}$, we have that $\widehat{\mathbf{D}} = \mathbf{M}^{-1}\mathbf{D}$. We obtain the global matrices from their element-wise counterparts, $\mathbf{M}^e$ and $\mathbf{D}^e$ (e stands for *element*), by direct stiffness summation, which maps the local degrees of freedom of an element Ω_e^h to the corresponding global degrees of freedom in Ω^h, and adds the element values in the global system. By construction, $\mathbf{M}$ is diagonal (assuming inexact integration), with an obvious advantage if explicit time integration is used.

In the discontinuous Galerkin approximation, the problem at hand is solved only locally and the flux integral that stems from the integration by-parts must be discretized as well. Because the current continuous/discontinuous Galerkin implementation is unified, we are effectively constructing flux integrals to build the boundary conditions for CG as well as DG. The element-wise counterpart of the matrix problem

(3) is then written as:

$$\frac{\partial \mathbf{q}^e}{\partial t} = -(\widehat{\mathbf{M}}^{\Gamma,e})^{\mathrm{T}} \breve{\mathbf{F}}(\mathbf{q}^e) + (\widehat{\mathbf{D}}^e)^{\mathrm{T}} \mathbf{F}(\mathbf{q}^e) + \mathbf{S}(\mathbf{q}^e), \tag{4}$$

where we obtain $\widehat{\mathbf{M}}^{\Gamma,e} = (\mathbf{M}^e)^{-1}\mathbf{M}^{\Gamma,e}$ from the element boundary matrix, $\mathbf{M}^{\Gamma,e}$, and the element mass matrix, $\mathbf{M}^e$. Out of various possible choices for the definition of the numerical flux $\breve{\mathbf{F}}(\mathbf{q})$ in Eq. (4), we adopted the Rusanov flux. We chose Rusanov for convenience; in previous work comparing HLL, HLLC, Roe, and Rusanov, we found no discernible differences in our results (albeit with a high-order triangular DG model). Although Rusanov is known to be too dissipative, at high-order (we used 4th or greater in this paper) it makes little difference. However, as shown in [61], the HLLC numerical flux contains an exact solution to the wet/dry problem, and so it should perform better especially at low order.

The Laplace operator of viscosity is approximated using the Symmetric Interior Penalty method (the reader is referred to [6] for details on its definition).

3.2. Time integration

Equation (3) is integrated in time by an implicit Runge-Kutta scheme that corresponds to the implicit part of the implicit-explicit scheme used in [25] (see also [12]). The method coefficients in standard ($A = a_{ij}$, b, c) tableaux form are the following

$$\begin{array}{c|ccc} 0 & 0 & & \\ 2-\sqrt{2} & 1-\frac{1}{\sqrt{2}} & 1-\frac{1}{\sqrt{2}} & \\ 1 & \frac{1}{2\sqrt{2}} & \frac{1}{2\sqrt{2}} & 1-\frac{1}{\sqrt{2}} \\ \hline & \frac{1}{2\sqrt{2}} & \frac{1}{2\sqrt{2}} & 1-\frac{1}{\sqrt{2}} \end{array}, \qquad \begin{array}{c|c} c & A \\ \hline & b \end{array}. \tag{5}$$

Scheme (5) is a three stage second order explicit-first-stage singly diagonally implicit Runge-Kutta (ESDIRK) scheme. This scheme has desirable accuracy and stability properties: (*i*) all stages are second order accurate, (*ii*) it is stiffly accurate and L-stable, and (*iii*) it is strong-stability-preserving [27] with coefficient of 2. These properties allow us to take large time-steps with high accuracy as well as alleviate the instability issues associated with sharp solution gradients [27]. The two-dimensional test presented later in this paper demonstrated to be the most demanding in terms of stability constraints. Method (5) allows us to gain up to one order of magnitude in terms of maximum admissible advective Courant number when compared to an explicit method (explicit part of ARK3, [35]). In particular, the explicit four-stage Runge-Kutta solution of the solitary wave against one isolated obstacle described in §6.4 preserved stability for up to Courant=0.21 using both CG and DG approximations. Although we were not able to use arbitrarily large time-steps with the ESDIRK with the current implementation (we will address this issue in a future work), we resolved the same problem at Courant=1.8. Schemes with a subset of these properties are employed by [34] and shown to be robust in this context. Method (5) used in this study satisfies all properties (*i*-*iii*).

Computationally, at each of the two implicit stages we have to solve a nonlinear equation $\mathbf{G}(\mathbf{Q}^{(i)}) = 0$, where $\mathbf{Q}^{(i)}$ are the stage values, $i = 2, 3$, and $\mathbf{G}$ is a linear combination of stage slopes with coefficients given in (5). We do so by using Newton iterations with a stopping criterion based on the relative decrease in the residual; that is, stop at iteration k if $||\mathbf{G}(\mathbf{Q}_k^{(i)})||/||\mathbf{G}(\mathbf{Q}_0^{(i)})|| < Tol_N$. At each Newton iteration we have to solve a linear system $\mathbf{J}(\mathbf{Q}_k^{(i)} - \mathbf{Q}_{k-1}^{(i)}) = -\mathbf{G}(\mathbf{Q}_{k-1}^{(i)})$, where $\mathbf{J}$ is the Jacobian matrix of $\mathbf{G}(\mathbf{Q}^{(i)})$. We approximate the Jacobian using directional finite differences and iterate with the generalized minimal residual (GMRES) method, which is effectively a Jacobian-free Newton–Krylov method [39]. The GMRES stopping criterion is also based on the relative residual. The first stage is explicit and equal to the last stage of the previous step, effectively making it a two-stage method, which saves some computational time.

4. The Shock Capturing Scheme

There are different ways to derive the viscous model described by Eq. (1) from the inviscid shallow water equations. Similarly to our previous work on the large eddy simulation of stratified atmospheric flows [48], the current model builds on the separation of scales between grid resolved (indicated as $\overline{f}(\mathbf{x})$ for any quantity $f(\mathbf{x})$) and unresolved (sub-grid). The unresolved scales are modeled via the shock capturing scheme at the core of this paper ($Dyn-SGS$).

Given an element Ω_e of order N and with side lengths $\Delta x, \Delta y$ of comparable size, we define the following characteristic length

$$\overline{\Delta} = \min(\Delta x, \Delta y)/(N+1). \tag{6}$$

The value of Δ sets the size of the smallest resolvable scales in the same way as cut-off filters do in large eddy simulation models.

The application of scale separation in the continuity equation (1a) results in the presence of an additional term on the right-hand side, which is the artificial viscosity term that appears in the equations (1). It is often debated whether artificial viscosity should be added to the continuity equation [53, 21, 30]; should the discrete viscous operator not be conservative, artificial viscosity must not be added to the continuity equation. However, by relying on spectral elements with integration by parts of the second-order diffusion operator, the discrete viscous operator is conservative, as shown in [29]. The numerical demonstration of conservation of the current approximation can be also found in our previous work [48] for the Euler equations. To get a sense of how necessary a stabilized continuity equation may be, we will show a few results for both conditions in §6.4.

Scale separation in the momentum equation yields a new equation that includes the gradient of the quantity

$$\boldsymbol{\tau}^{SGS} \approx \overline{H}\mu_{SGS}\nabla\overline{\mathbf{u}}. \tag{7}$$

The coefficient μ_{SGS} is defined element-wise and is given as:

$$\mu_{SGS} = \max\left(0.0, \min(\mu_{\max}|_{\Omega_e}, \mu_{\text{res}}|_{\Omega_e})\right), \tag{8}$$

where

$$\mu_{\text{res}}|_{\Omega_e} = \overline{\Delta}^2 \max\left(\frac{\|R(H)\|_{\infty,\Omega_e}}{\|H-\widehat{H}\|_{\infty,\Omega}}, \frac{\|R(H\mathbf{u})\|_{\infty,\Omega_e}}{\|H\mathbf{u}-\widehat{H\mathbf{u}}\|_{\infty,\Omega}}\right) \tag{9}$$

and

$$\mu_{\max}|_{\Omega_e} = 0.5\overline{\Delta}\left\||\mathbf{u}| + \sqrt{gH_s}\right\|_{\infty,\Omega_e}. \tag{10}$$

In (9, 10), $\widehat{\cdot}$ indicates the spatially averaged value of the quantity at hand over the global domain Ω, the norms $\|\cdot\|_{\infty,\Omega}$ at the denominator are used to preserve the physical dimension of the resulting equation, and $R(H)$ and $R(H\mathbf{u})$ are the residuals of the inviscid governing equations. At each time-step, the residuals are known and given by:

$$R(H) = \frac{\partial H}{\partial t} + \nabla\cdot(H\mathbf{u}), \tag{11a}$$

$$R(H\mathbf{u}) = \frac{\partial H\mathbf{u}}{\partial t} + \nabla\cdot\left(H\mathbf{u}\otimes\mathbf{u} + \frac{g}{2}(H^2 - H_b^2)\mathbf{I}\right) + gH_s\nabla\cdot(H_b\mathbf{I}). \tag{11b}$$

The presence of R makes the artificial viscosity mathematically consistent, which means that the residual-based viscosity vanishes when the residual is zero. The quantity $|\mathbf{u}| + \sqrt{gH_s}$ in (9, 10) is the maximum wave speed.

We would like to emphasize the necessity for the physically correct dimensions of the viscosity coefficient. This is an important issue that is often underestimated and not accounted for in the design of artificial viscosity methods for stabilization purposes.

As previously underlined in [48], the most important aspect of $Dyn-SGS$ for high-order solutions is its ability to prevent spurious oscillations without the necessity of additional low-pass filters or limiters. This fact is even more important when we rely on DG to solve the shallow water equations on wet and dry surfaces; as pointed out in [36], an improper and unnecessary use of the limiter, coincidentally may even destroy the conservative properties of the DG predictions rather than improving them. In this paper we concentrate on using $Dyn-SGS$ to remove spurious oscillations in the proximity of the propagating bores and see how much we can rely on it without depending on auxiliary filters and limiting mechanisms.

This model is based on a second-order Laplacian operator; it is not expensive and does not add additional burden in parallel. However, the dynamic coefficient depends on an infinity norm, which may become an issue in parallel as one global communication is necessary. To minimize this cost, one option that we tested in previous work is to build the viscosity only at certain time-steps. The potential user of this model may want to explore its algorithmic optimization.

5. Wetting and drying

It is difficult to include wetting and drying algorithms while preserving high-order accuracy. The application of wetting/drying with discontinuous Galerkin using low-order Lagrange polynomials was proposed by several authors [11, 64, 34, 28], and using Bernstein polynomials up to order three in [7]. The positivity preserving limiter of Xing et al. [65] was designed for high-order discontinuous Galerkin to solve this problem in particular. In this paper, we do not investigate advanced options in this respect and rely on the presence of a relatively small layer of water in the regions that should be dry, and apply the limiter by Xing et al. whenever the dynamic viscosity is not sufficient to preserve stability at the wet/dry interface.

6. Numerical tests

We verify the correctness of our models through a set of one- and two-dimensional tests. These are the classical dam break on a wet surface (also known as the Sod's tube problem in the literature of gas dynamics). The second test is the tsunami run-up on a sloping beach, which is followed by the standard problem of an oscillating lake in a parabolic bowl. In 2D we analyze a test that includes all of the features of the previous 1D tests. This test consists of a complex flow of interacting waves triggered by a dam breaking on a lake surface; furthermore, the interacting waves impinge against an initially dry isolated obstacle.

6.1. Dam break

We study the problem of a dam breaking on a wet surface [57] in the 1D domain $\Omega = x = [-5, 5]$ m with solid boundaries. This particular problem does not involve a wet/dry surface, and hence allows us to only rely on $Dyn-SGS$ for stabilization purposes without the necessity of additional filters or limiters. For this reason, this test is useful to isolate the action of $Dyn-SGS$ alone in the proximity of strong fronts. This special case of a Riemann problem gives rise to the propagation of a rarefaction wave (depression) that moves leftward towards the deep water and a shock wave (bore) that moves rightward into a shallow water region. Given the water depths h_L and h_R on the left and right of the dam initially centered at $x_0 = 0$ m, the initial water level of the problem is given by

$$H(\mathbf{x},0) = \begin{cases} h_L = 3 & \text{if } x < x_0 \\ h_R = 1 & \text{if } x > x_0 \end{cases}$$

whereas velocity is zero everywhere. The exact solution to this problem can be computed with the method of characteristics (see, [61, 43]). The exact solution of the water level is given by [17]:

$$H(\mathbf{x},t) = \begin{cases} h_L & \text{if } x < x_A(t) \\ \frac{4}{9g}\left(\sqrt{gh_L} - \frac{x}{2t}\right)^2 & \text{if } x_A(t) \le x \le x_B(t) \\ \frac{c_m^2}{g} & \text{if } x_B(t) \le x \le x_C(t) \\ h_R & \text{if } x \le x_C(t) \end{cases}$$

where

$$\begin{cases} x_A(t) = x_0 - t\sqrt{gh_L} \\ x_B(t) = x_0 + t\left(\sqrt{gh_L} - 3c_m\right) \\ x_C(t) = x_0 + t\frac{2c_m^2\left(\sqrt{gh_L} - c_m\right)}{c_m^2 - gh_R}. \end{cases}$$

and $c_m = 1.848 \mathrm{m}\, s^{-1}$ [17].

In Figure 1 we plot the exact and numerical solutions at $t = 0.1$ s and $t = 0.5$ s. The numerical solutions are those computed using CG and DG with and without artificial viscosity. Neither computation uses filters or limiters so that we can isolate the effects of $Dyn-SGS$ on the solution. Without $Dyn-SGS$, the CG solution loses stability almost immediately. In the case of DG, the Gibbs oscillations triggered by the moving bore propagate upstream as the front moves. These modes are removed by including $Dyn-SGS$ to the mass and momentum equations.

Because we added artificial viscosity to the continuity equation, we verify that the model did not violate mass conservation. As we mentioned in the introduction, the use of diffusion in the continuity equation is often an issue of disagreement among researchers. We demonstrated in [48] that mass can be conserved for the Euler equations when $Dyn-SGS$ is applied. In figure 2 we plot the evolution of the relative mass loss for the dam break problem. The relative mass loss is defined as

$$M(t)_{loss} = \frac{\int_x \left[H(x,t) - H(x,t_0)\right] dx}{\int_x H(x,t_0) dx}. \tag{12}$$

From figure 2 we observe that mass loss is minimal when DG is used. Although it is still small and lies in the range of machine precision, conservation worsens for CG. This finding agrees with [41], although it was proved in that paper that CG and DG should be equally conservative.

To avoid compounding roundoff errors in the computation of mass error, we use a pairwise summation algorithm to add up mass contributions from all grid points [41]. In a regular sum operation, we add a big number of contributions one-by-one which, eventually, results in adding a relatively small number to a big partial sum. In other words, the sum $S = a_1 + a_2 + ... + a_n$ consists of $S = a_1 + a_2$, followed by $S = S + a_3$ and so on to $S = S + a_n$. For a large number of these summations, the partial sum

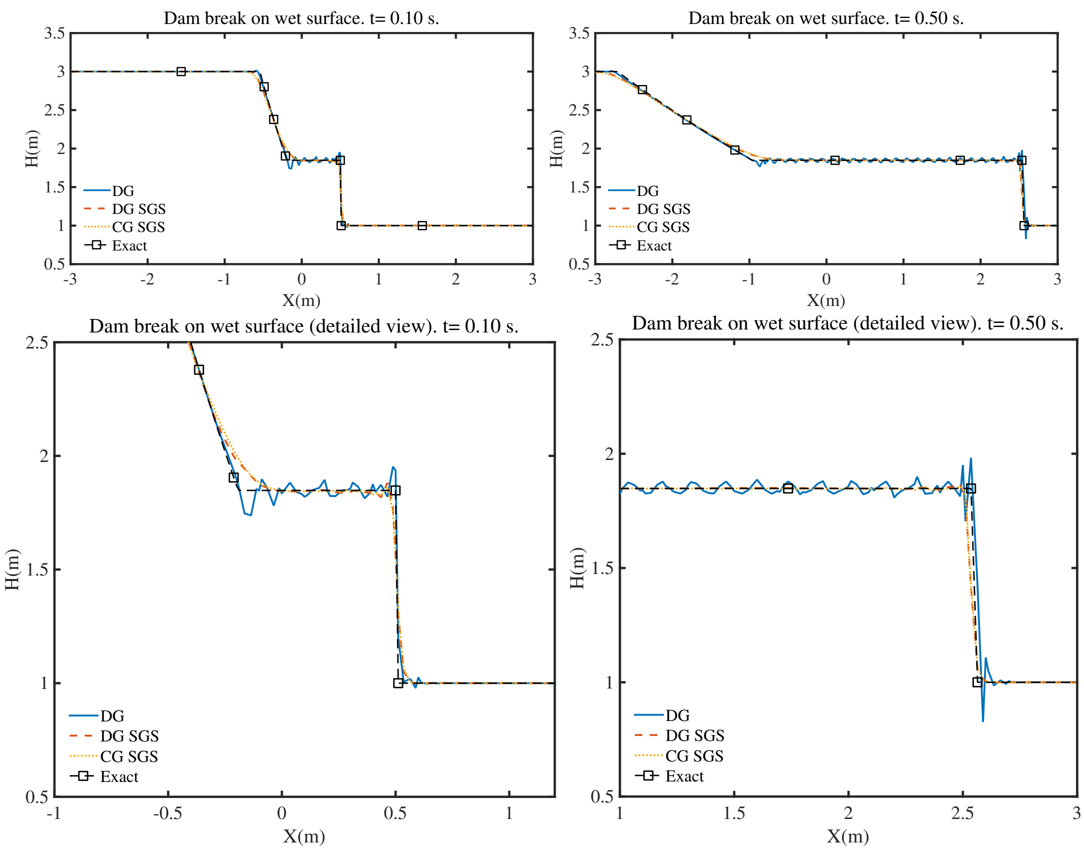

Figure 1: Dam break on wet surface. Water surface using CG and DG with and without dynamic viscosity for the full domain (top) and in the proximity of the bore (bottom). The CG solution could only be calculated with the help of viscosity.

S eventually becomes much larger than the contributions a_i, which hence lead to important roundoff errors. In the pairwise summation algorithm we add two similar numbers at a time and then recursively add the partial results in the same fashion. The computation of S is split into $S_1 = a_1 + a_2$, $S_2 = a_3 + a_4$, ..., $S_{n/2} = a_{n-1} + a_n$, and then recursively the partial sums are added in the same way to form the total sum S. With this approach, we always add numbers of similar magnitudes, which significantly reduces roundoff errors. This algorithm is key if incorporated within algorithms that are expected to conserve mass up to machine precision.

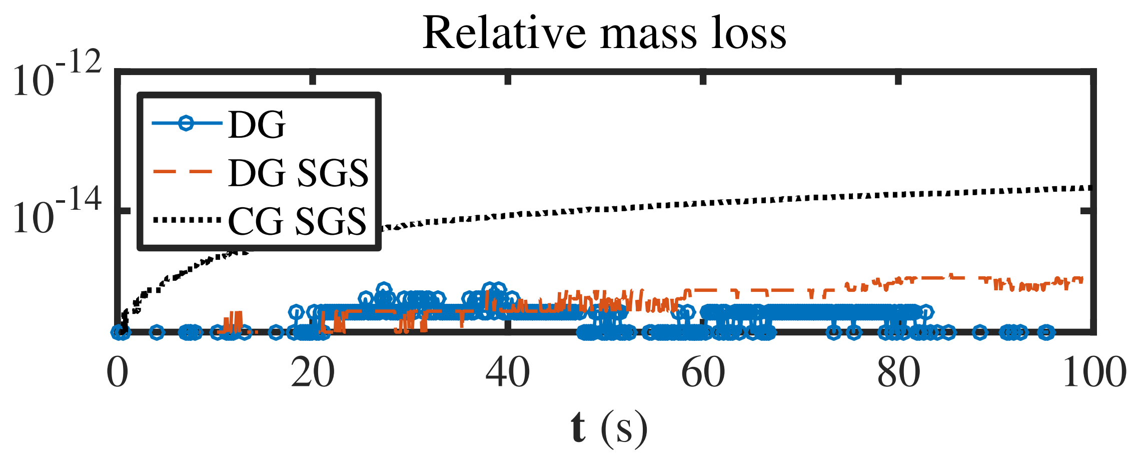

Figure 2: Relative mass loss computed in the dam break problem. This test was run without any limiters to fully assess the stabilization properties of $Dyn-SGS$. The CG solution could only be calculated with the help of viscosity.

6.2. 1D tsunami run-up over a sloping beach

The run-up of a long wave on a uniformly sloping beach was originally proposed as a benchmark for shallow water codes at the third international workshop on long-wave run-up models [1]. The one-dimensional computational domain is defined as $\Omega = x = [-500, 50000]$ m. The dry initial beach is 500 m long. The initial waveform was defined by Carrier et al. in [13] for an $L = 8$ m domain as:

$$\eta = a_1 \exp\{-\hat{k}_1(x-\hat{x}_1)^2\} - a_2 \exp\{\hat{k}_2(x-\hat{x}_2)^2\}, \tag{13}$$

with constants $(a_1, a_2, \hat{k}_1, \hat{k}_2, \hat{x}_1, \hat{x}_2) = (0.006, 0.018, 0.4444, 4.0, 4.1209, 1.6384)$. To scale the wave to the $L = 50000$ m long domain used for the current test, we introduced the scaling factor $\xi = L/8$ and re-expressed Eq. (13) with respect to $x_{1,2} = \hat{x}_{1,2}\xi$ and $k_{1,2} = \hat{k}_{1,2}/\xi^2$; we utilize larger amplitudes $(a_1, a_2) = (3.0, -8.8)$. The initial wave is plotted in Fig. 3.

We plot the CG solutions at times $t = [160, 175, 220]$ s in Fig. 4 and compare them

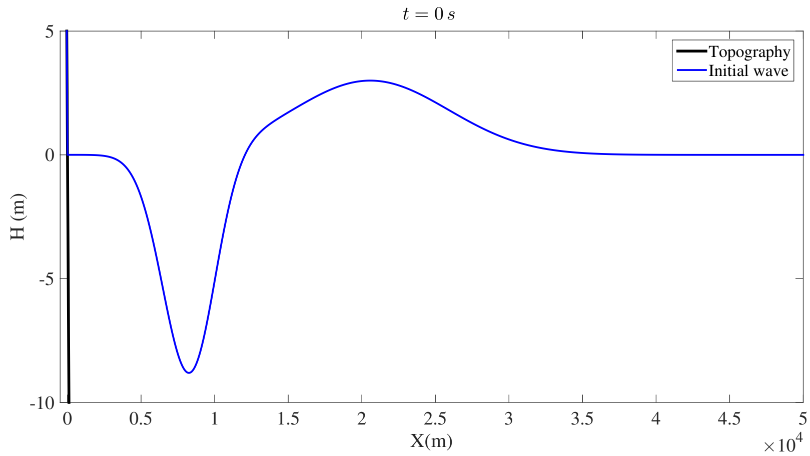

Figure 3: Far-field plot of the initial Carrier's N-wave for the 1D tsunami run-up problem.

against the tabulated data available in [1]. Fig. 4 shows that the effect of viscosity on the water surface solution is clearly negligible. This can be explained by looking at the structure and values of μ_{SGS} in Fig. 5. With a water surface that is smooth almost everywhere, the dynamically adaptive viscosity coefficient is so small that its effect becomes minimal. We will see later that this will not be the case in problems with a greater degree of irregularity of the surface. We do not show the DG version of the solution because the differences with respect to the CG solution are negligible. The plots on the right hand side column show, on the other hand, that the velocity field features oscillations at the point of transition from fully wet to dry.

In the left plot of Fig. 6 we show the solution of the wave elevation in the $x-t$ plane, whereas on the right of the same figure we plot the total depth and the time evolution of the shoreline. The dashed red curve in the right plot represents the tabulated shoreline available in [1]. By direct comparison with Carrier's results [13], the patterns of the water surface elevation ($\eta(x,t)$) and total water depth are in full agreement. As mentioned above, we rely on a thin layer (1e-3 m in this case) of water in the regions that should be dry.

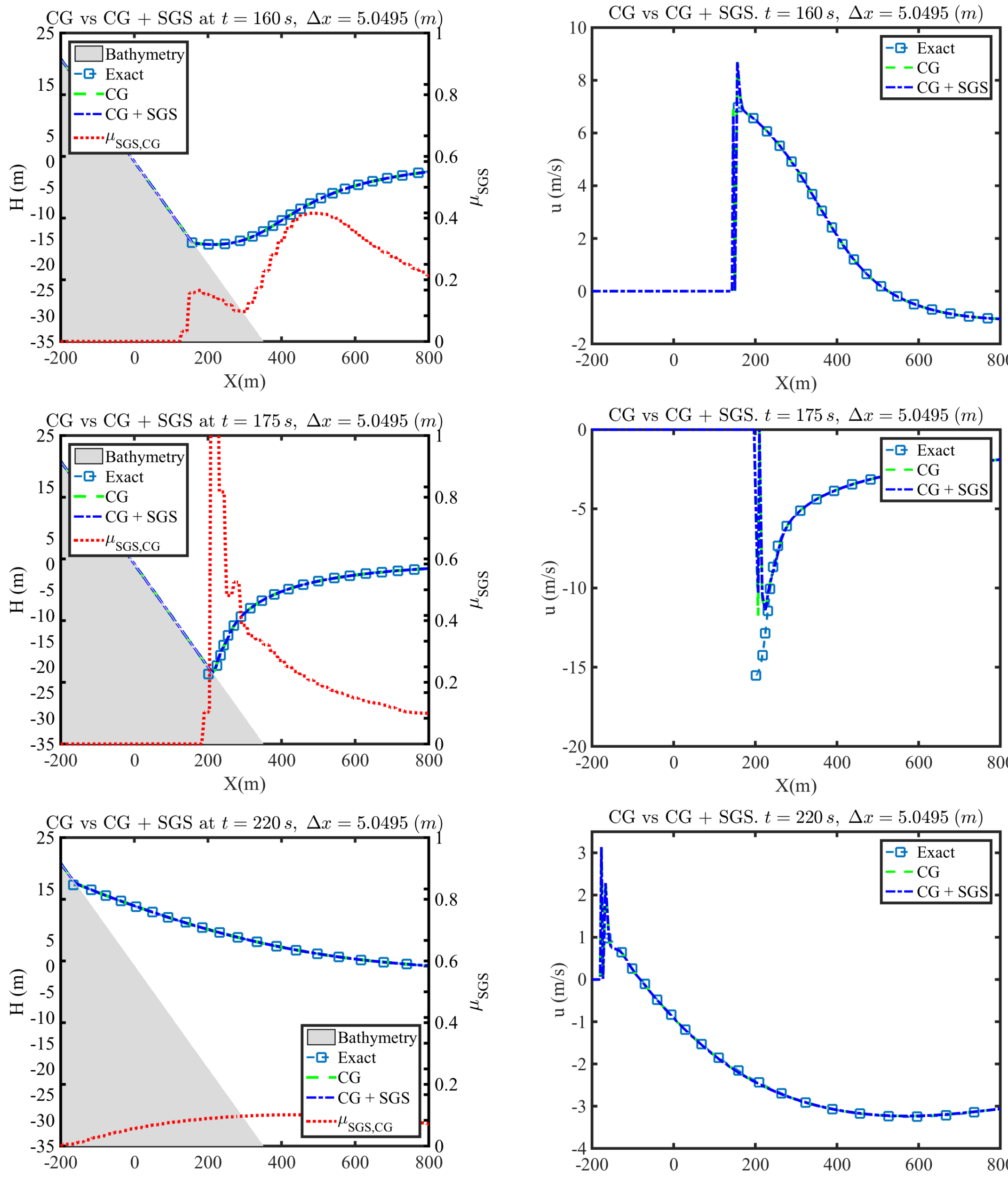

Figure 4: 1D tsunami run-up as computed with CG with and without artificial viscosity. Near field plot of the solutions at $t = [160, 175, 220]$ s. In the left column we plot the water surface and the distribution of μ_{SGS}. We plot velocity on the right column. The problem is smooth almost everywhere so that the intensity of the adaptive viscosity is minimal.

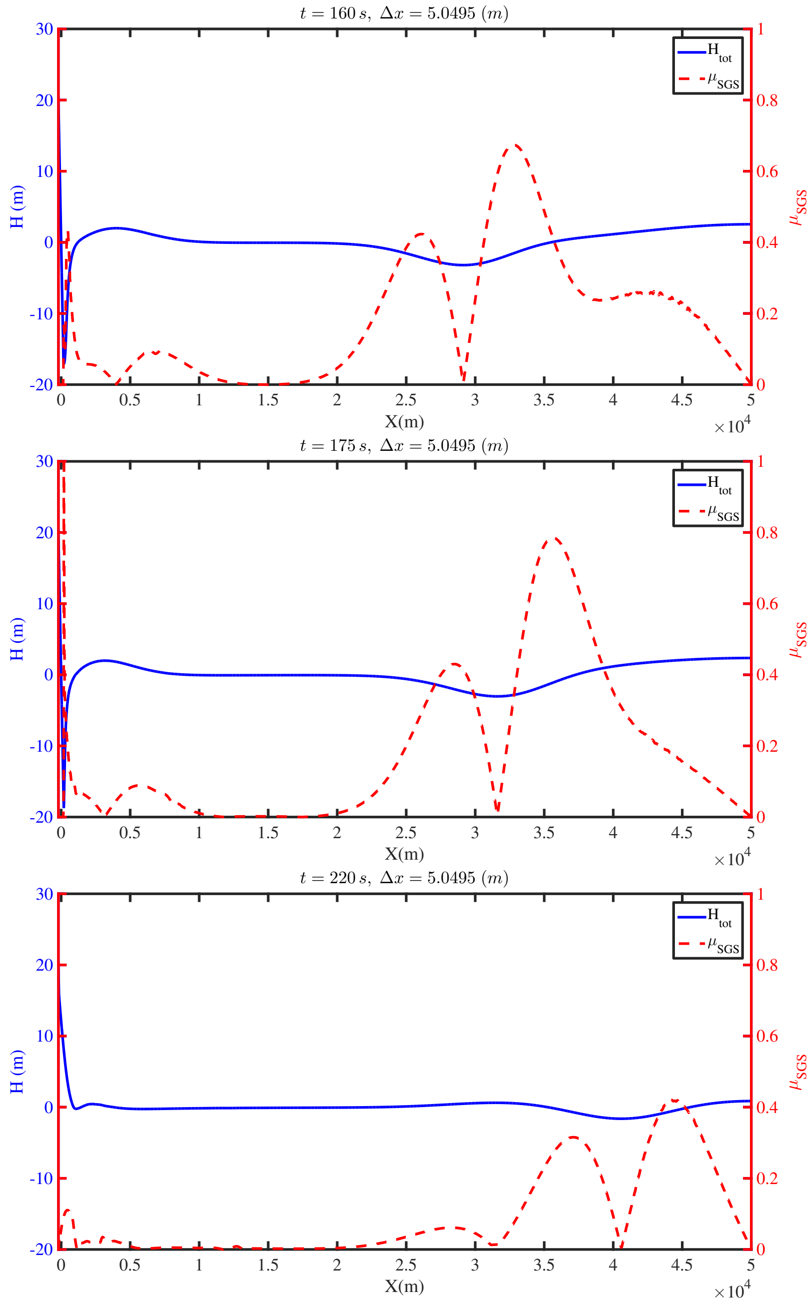

Figure 5: Far field plot of dynamic μ_{SGS} (red, dashed line) and water surface (blue, solid line) in the full domain for the 1D tsunami run-up over a sloping beach. The effect of viscosity on the solution of Fig. 4 is minimal as the value of the coefficient is indeed very small. The solution is smooth almost everywhere, which is the reason for the very small values of μ_{SGS}.

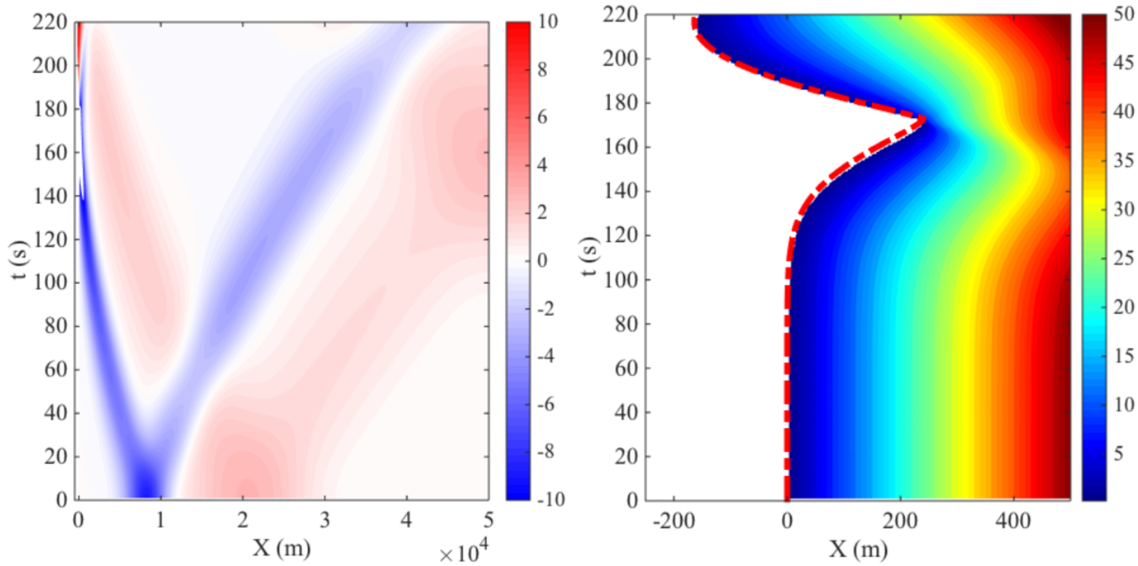

Figure 6: 1D tsunami run-up over a sloping beach. Left: wave trajectory (characteristic curves) in the full 50 km long domain. Right: $x-t$ variation of the water depth (H_s+H_b) in the proximity of the coast. The shoreline is at the interface between the white area (dry shore) and the color shading (water surface). The dashed red curve is the exact shoreline.

6.3. 1D test with analytic solution

To measure the convergence rate of the model, we compare the computed solutions against the analytic solution of the flow in a one-dimensional parabolic bowl [19, 60]. The parabolic topography is defined as:

$$H_b(x) = h_0\left(\frac{1}{a^2}x^2\right) - 0.5 \tag{14}$$

where $h_0 = 2$ m and $a = 1$ in $\Omega = x = [-1, 1]$ m. The initial velocity is $u = 0\,\mathrm{ms}^{-1}$ and the water surface begins to oscillate due to gravity only. The solution is computed using 16, 32, 64, and 128 elements of order 4. Figs. 7-9 show these solutions obtained with and without $Dyn-SGS$ for both CG and DG. The contribution of the artificial viscosity is evident at all resolutions by looking at the detailed views in the figures.

As the grid is refined, the unstabilized solutions behave sufficiently well in spite of minor oscillations that are immediately removed by the addition of viscosity. It is evident that the DG solution outperforms the CG solution in all cases in terms of stable water surface and momentum (see momentum in Fig. 10). To quantify the difference between the stabilized and unstabilized solutions, we plot the normalized L_2 error norms in Fig. 11. In the figure, we notice that the slope of the stabilized CG solution is greater than its unstabilized counterpart, although the same does not occur in the case of DG. By observing that both CG and DG seem to require artificial viscosity for a better solution as discussed above, we require further analysis on this point to find a possible reason for this behavior. We leave this for a future paper where we are planning on analyzing the effect of different inundation schemes as well.

6.4. 2D solitary wave run-up and run-down on a circular island

A solitary wave run-up on a circular island was studied in [10] at the Waterways Experiment Station of the US Army Corps of Engineers. In this example, the initial wave is modeled via the following analytic definition by Synolakis [58]:

$$\eta(\mathbf{x},0) = \frac{A}{h_0}\mathrm{sech}^2\left(\gamma(x-x_c)\right), \tag{15}$$

where $A = 0.064$ m is the wave amplitude, $x_c = 2.5$ m, $h_0 = 0.32$ m is the initial still water level, and

$$\gamma = \sqrt{\frac{3A}{4h_0}}. \tag{16}$$

The island is a cone given as

$$H_b = 0.93\left(1-\frac{r}{r_c}\right), \quad \text{if } r \leq r_c, \tag{17}$$

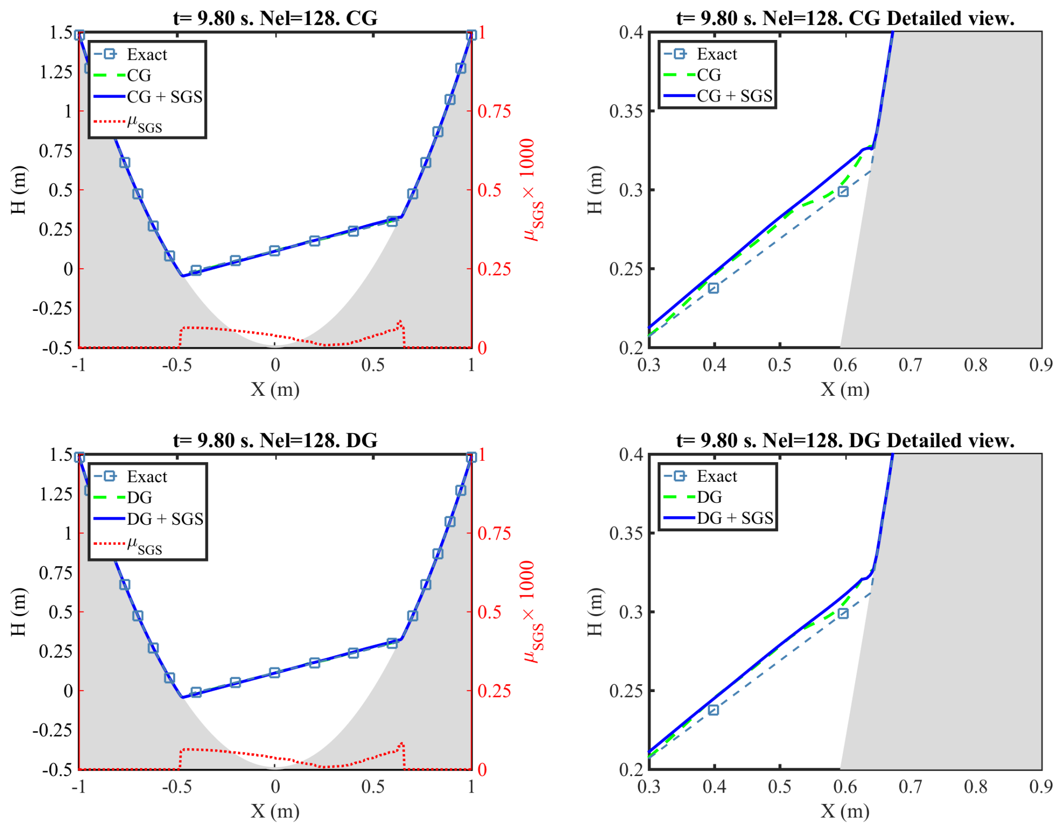

Figure 7: 1D flow in a parabolic bowl. Fine grid **CG** (top row) and **DG** (bottom row) solutions with and without artificial viscosity. The far field view is plotted on the left column whereas the detailed view of the wet/dry front in on the right. Computed water level without $Dyn - SGS$ (green, dashed line), with $Dyn - SGS$ (blue, solid line), exact solution (steel blue, dashed with open squares), and μ_{SGS} (red, solid line). For visualization, μ_{SGS} is scaled by a factor of 1000. *Notice:* μ_{SGS} is piece-wise constant by construction; however, its distribution sometimes appears to be partially piece-wise linear; this is caused by the data interpolation from the high-order grid to a linear grid necessary for plotting purposes via Matlab.

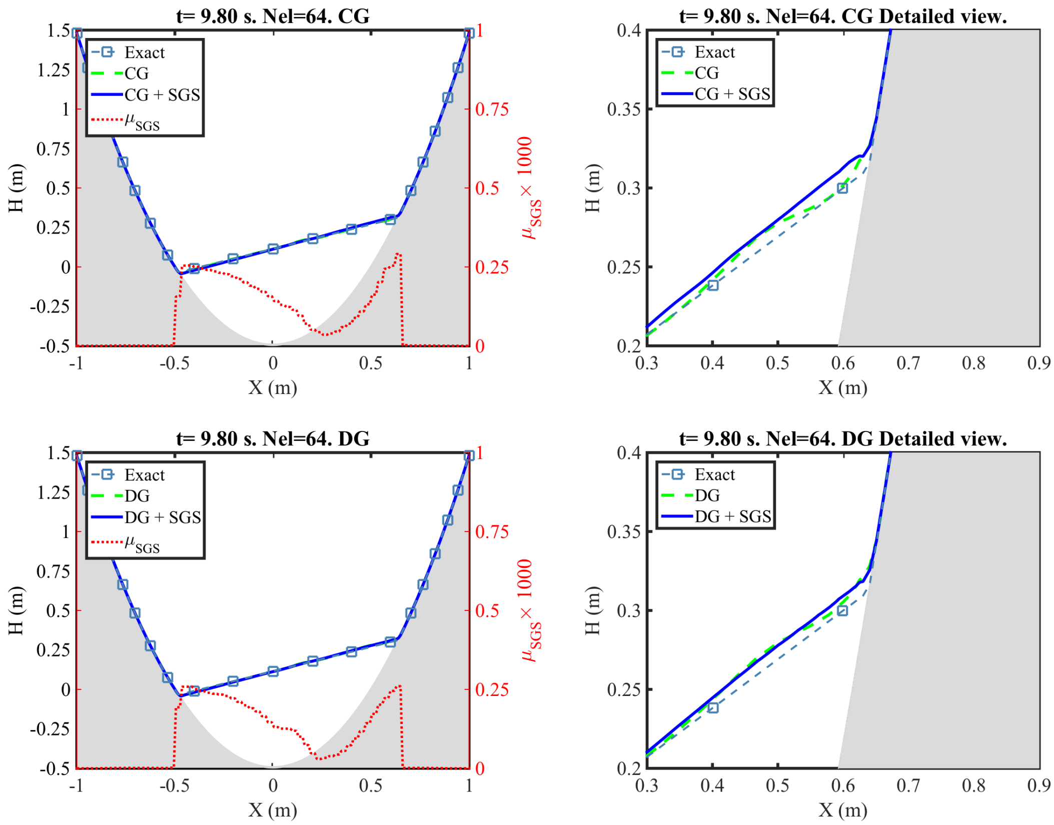

Figure 8: 1D flow in a parabolic bowl. Like Fig. 7 but two times coarser.

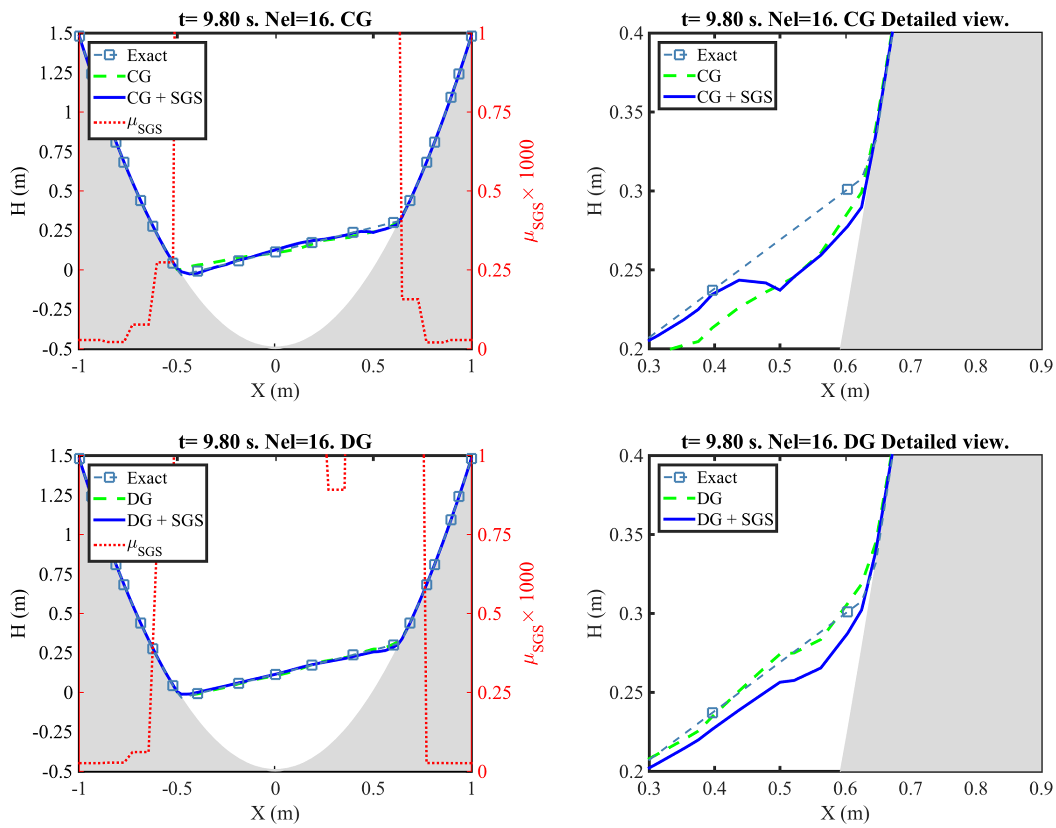

Figure 9: 1D flow in a parabolic bowl. Like Fig. 7 but eight times coarser.

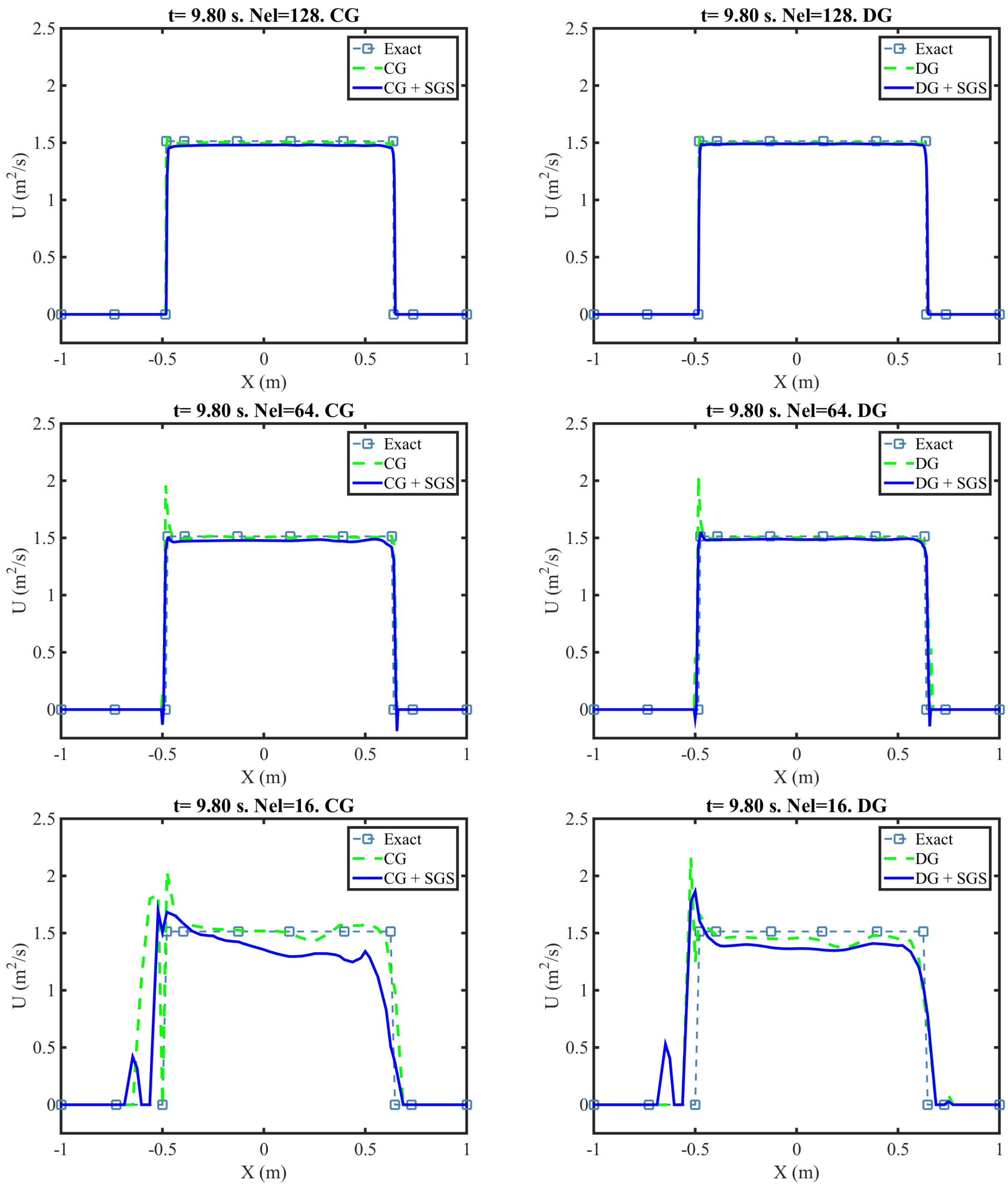

Figure 10: 1D flow in a parabolic bowl. Momentum at three different resolutions using CG (left column) and DG (right column).

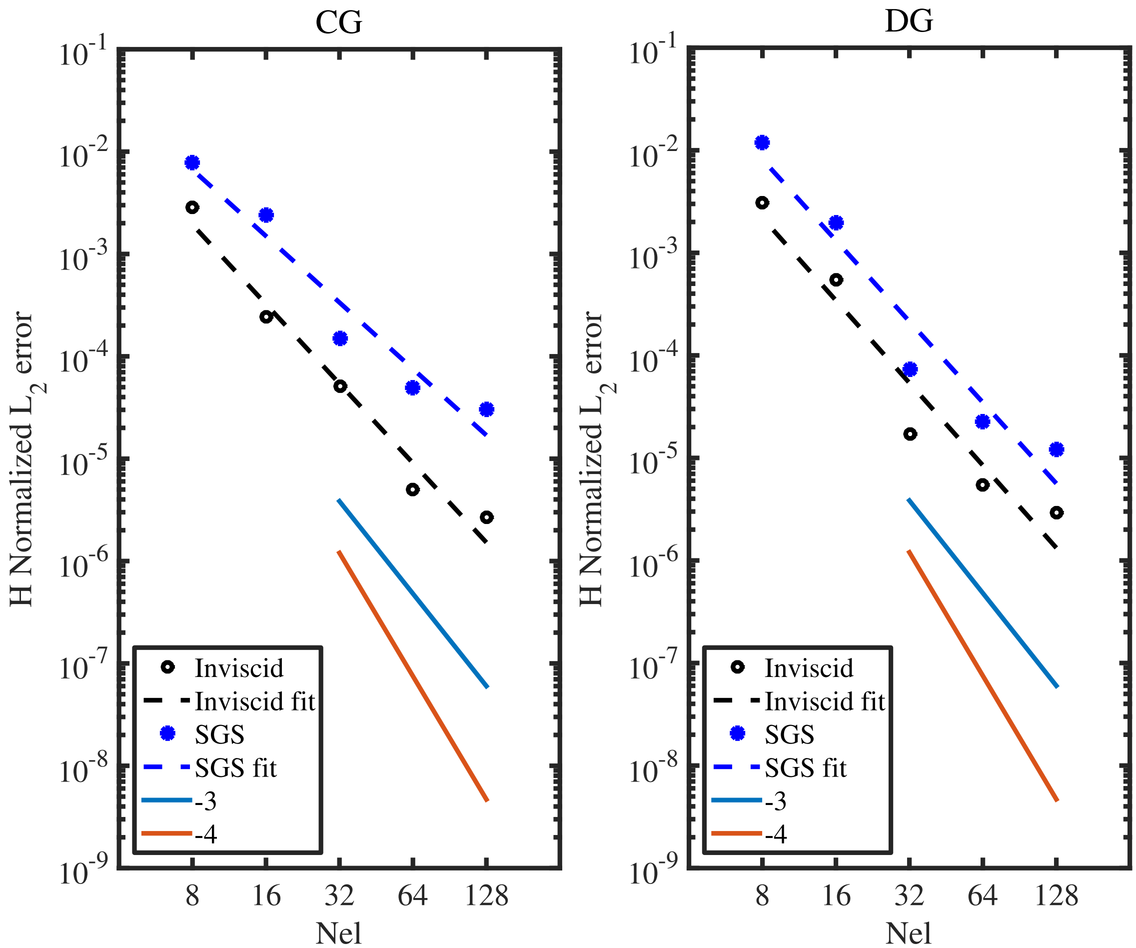

Figure 11: Normalized L_2 error of water surface at $t = 10$ s for **CG** (left) and **DG** (right). The -3 and -4 curves indicate the reference rates.

where $r = \sqrt{(x-x_c)^2+(y-y_c)^2}$, $r_c = 3.6$ m, and is centered at $(x_c, y_c) = (12.5, 15)$ m. The cone is mounted on a flat bathymetry. The fluid is confined within four solid walls.

To understand how the proposed adaptive viscosity and numerical approximation depend on the grid, we ran the simulation at the four resolutions $\Delta\mathbf{x} \approx [0.05\,, 0.10\,, 0.20\,, 0.40]$ m. Fig. 12 shows that the stabilized DG solution is converging to the same solution and the main features of the interacting waves are reproduced almost equally across the four grids. Certainly, the 0.40 m grid spacing is the most dissipative, although it is encouraging to see how the important features resolved at 5 cm are still well represented on the coarsest grid. The same observation applies to the CG solution (plot not shown).

In Figs. 13-16 we plot the projection of the 2D solution on the plane $y = 0$. The spurious modes that characterize the water surface in the proximity of the sharpest wave front are fully removed by $Dyn-SGS$ (Figs. 13, 14) without noticeably weakening the front sharpness. This is in full agreement with the application of $Dyn-SGS$ to non-linear wave problems with strong discontinuities, as previously shown in [48, Figs. 16, 17] for the solution of the Burgers' equation. We briefly mentioned above how DG already has built-in viscosity. This is clearly visible from the plot of Fig. 14; the unstabilized DG solution shows no oscillations except for, at most, some minimal under- and over-shooting. This implies that the numerical residual of the DG approximation is so small that the effect of the shock capturing model reduces to a minimum value. This explains why the inviscid and viscous DG solutions look similar.

In Fig. 15 we compare the unstabilized (left plot) against the stabilized (right plot) CG solutions for velocity. We show the same comparison for DG in Fig. 16.

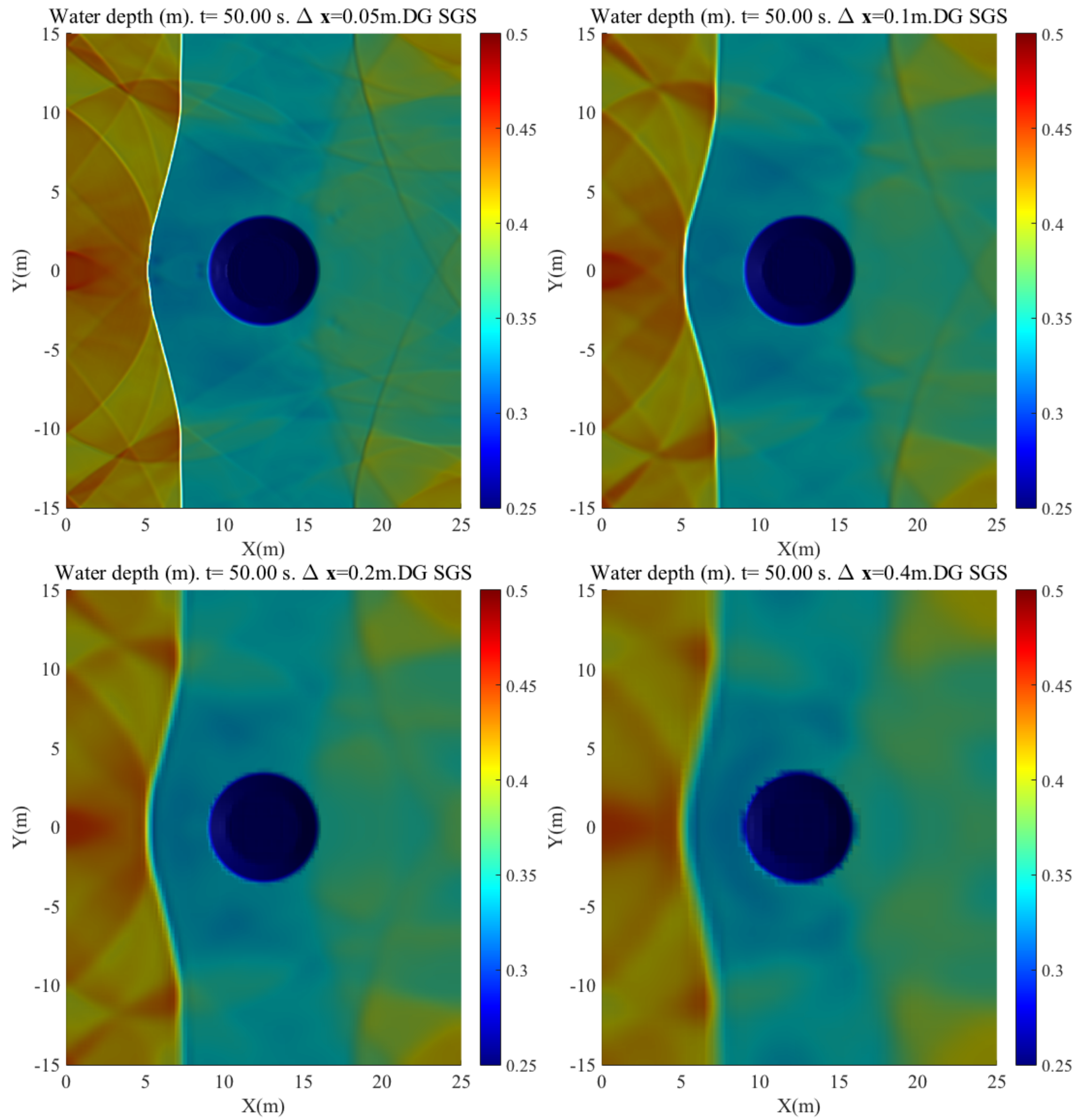

Figure 12: **DG** solution of water depth for the single-hill configuration. Results obtained with the four grid resolutions $\Delta\mathbf{x} = [0.05, 0.10, 0.20, 0.40]$ m (indicated in the figures) using 4^{th}-order elements. The color bar is cut at 0.25 to preserve the visibility of the smallest features. The dark blue coloring within the region of the cone corresponds to the water depth equal to the threshold water layer of 1e-3 m.

Unlike for the case of the water surface, for both CG and DG we notice a great difference between the stabilized and unstabilized solutions. However, this is not telling us anything about the correctness of the solution since this two-dimensional problem is non-linear, has multiple interacting waves, and does not have an analytic solution for the velocity field. On the contrary, what we can tell is that the effect of $Dyn-SGS$ on the CG solution is consistent with its effect on the DG solution; the stabilized CG and DG solutions plotted in the right plots of Figures 15 and 16 show similar wave fronts. This is indicative of a correct implementation of the unified CG/DG framework. By looking at the 3D velocity plots in Fig. 17, we observe that the greatest difference between the unstabilized (top) and stabilized (bottom) velocities occurs in a narrow region by the plane $y = 0$ up- and down-wind of the obstacle. As we move farther and farther towards $y > 0$, the velocity fields are in much greater agreement with each other, as it is visible by observing the position and strength of the wave fronts across the domain in both plots.

Theoretically, two numerical methods should produce identical results under the constraint of zero numerical error. This is not practically true and small dispersion errors may be still expected as long as they are sufficiently small. This test is meant to demonstrate that $Dyn-SGS$ does not damp the solution as time evolves (this test ran for 50 seconds), which is an important requirement for dissipation based stabilization methods.

We computed the solutions plotted in Fig. 18 applying the shock capturing to the continuity ($\delta = 1$ in Eq. (1)) and momentum equations. When compared against the unstabilized solution (bottom plot in the same figure), we notice that the features of the fronts of the interacting waves are fully preserved. Furthermore, the fronts are not excessively smeared out as the high frequency modes are removed.

We show the instantaneous energy spectra of the stabilized and unstabilized CG

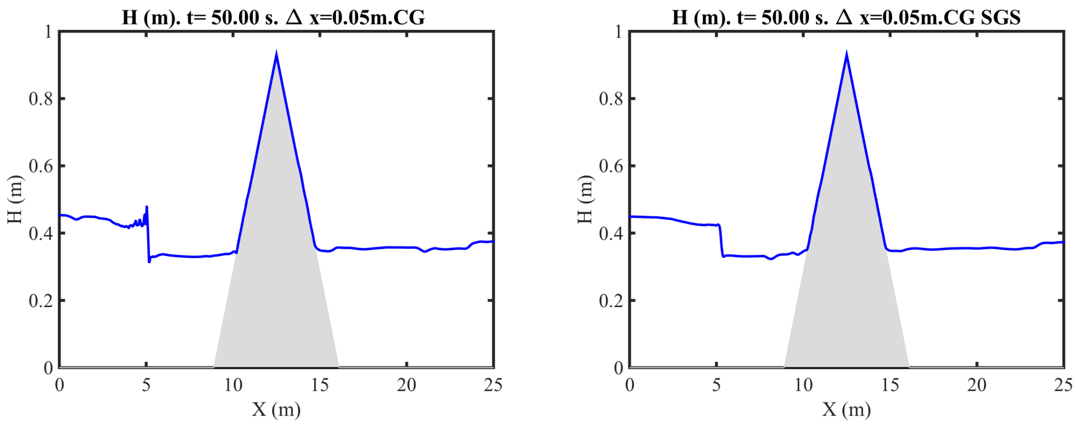

Figure 13: $x - z$ vertical slice of the 2D **CG** solution of water depth (H) for the single-hill configuration. Inviscid (left) against stabilized solution using SGS (right). Solutions obtained using 4^{th}-order elements. The dark blue coloring within the region of the cone corresponds to the water depth equal to the threshold water layer of 1e-3 m.

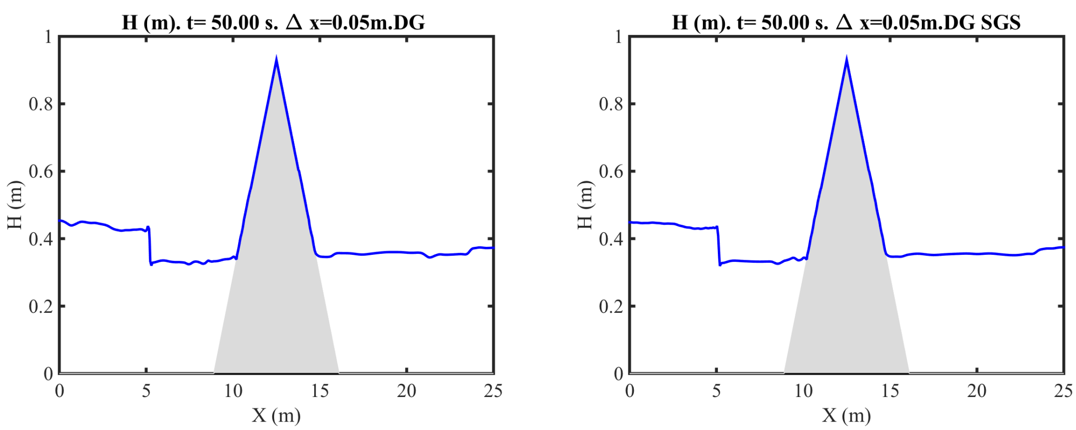

Figure 14: Like Fig. 13 but for **DG**. The dark blue coloring within the region of the cone corresponds to the water depth equal to the threshold water layer of 1e-3 m. This plot shows the power of DG. Without SGS it still almost captures the bore sharply.

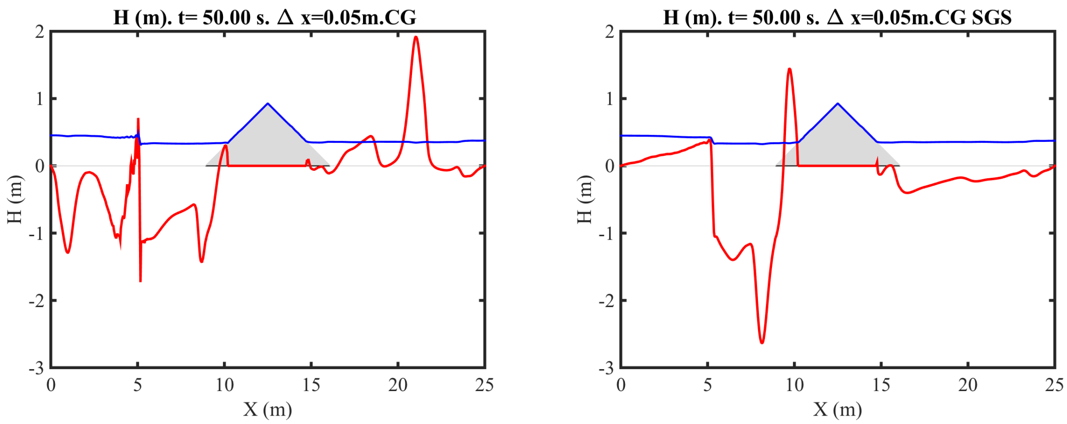

Figure 15: $x-z$ view of the 2D **CG** velocity solution (red curve) superimposed to the water surface (blue curve). The inviscid solution is shown on the left.

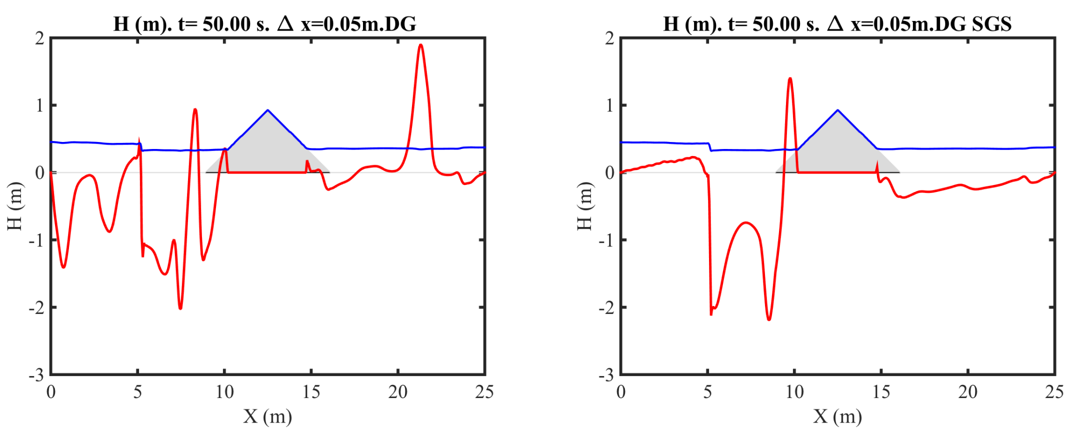

Figure 16: Like Fig. 15, but using **DG**.

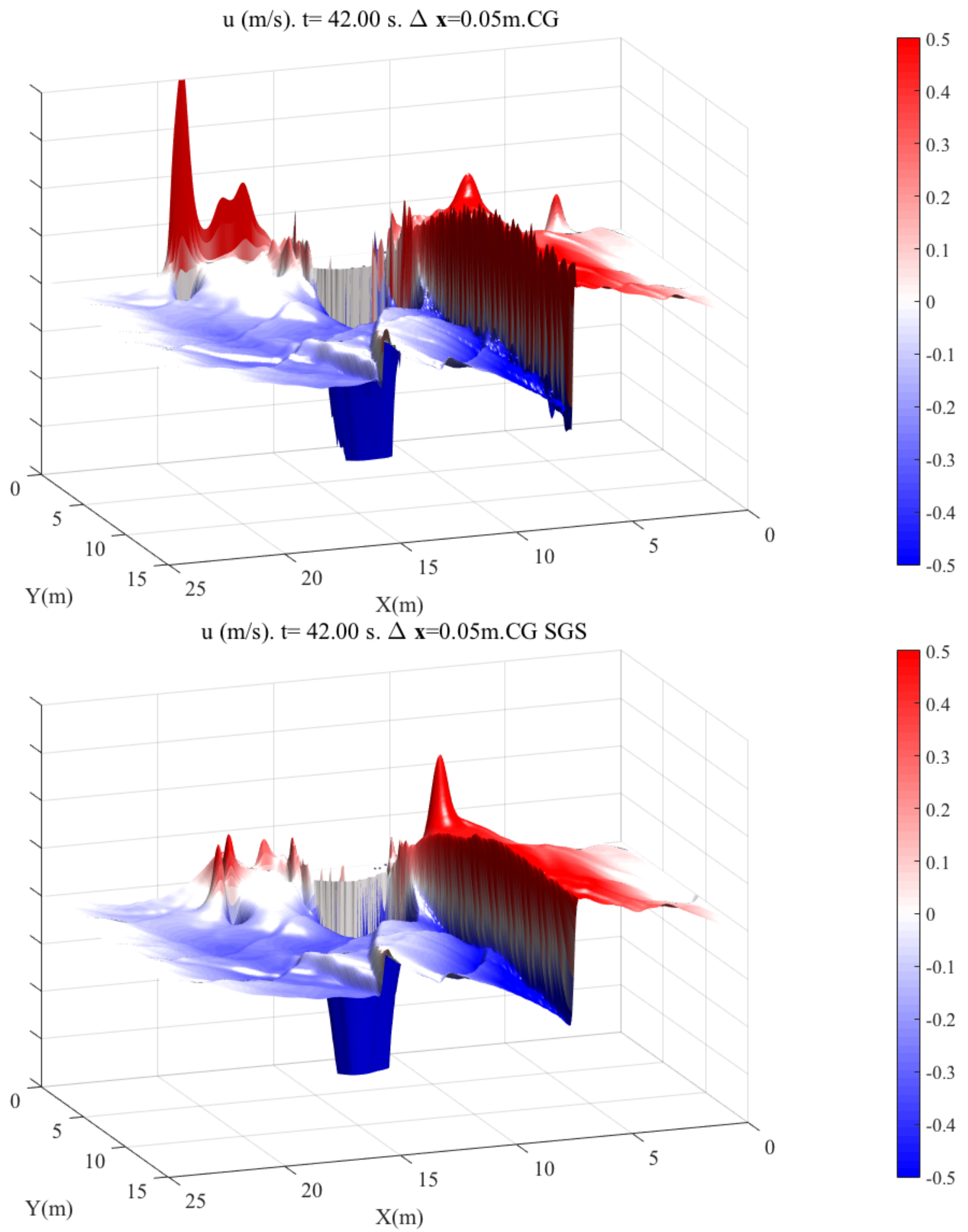

Figure 17: Instantaneous perspective view of the unstabilized (top) and stabilized (bottom) **CG** solutions of the velocity for $\Delta\mathbf{x} = 5$ cm using 4^{th}-order elements. We observe that the greatest difference between the unstabilized (top) and stabilized (bottom) velocities occurs in a narrow region by the plane $y = 0$ up- and down-wind of the obstacle. As we move farther and farther towards $y > 0$, the velocity fields are in much greater agreement with each other, as it is visible by observing the position and strength of the wave fronts across the domain in both plots. For best view of the velocity surface, the view angle is different from the one of Fig. 18.

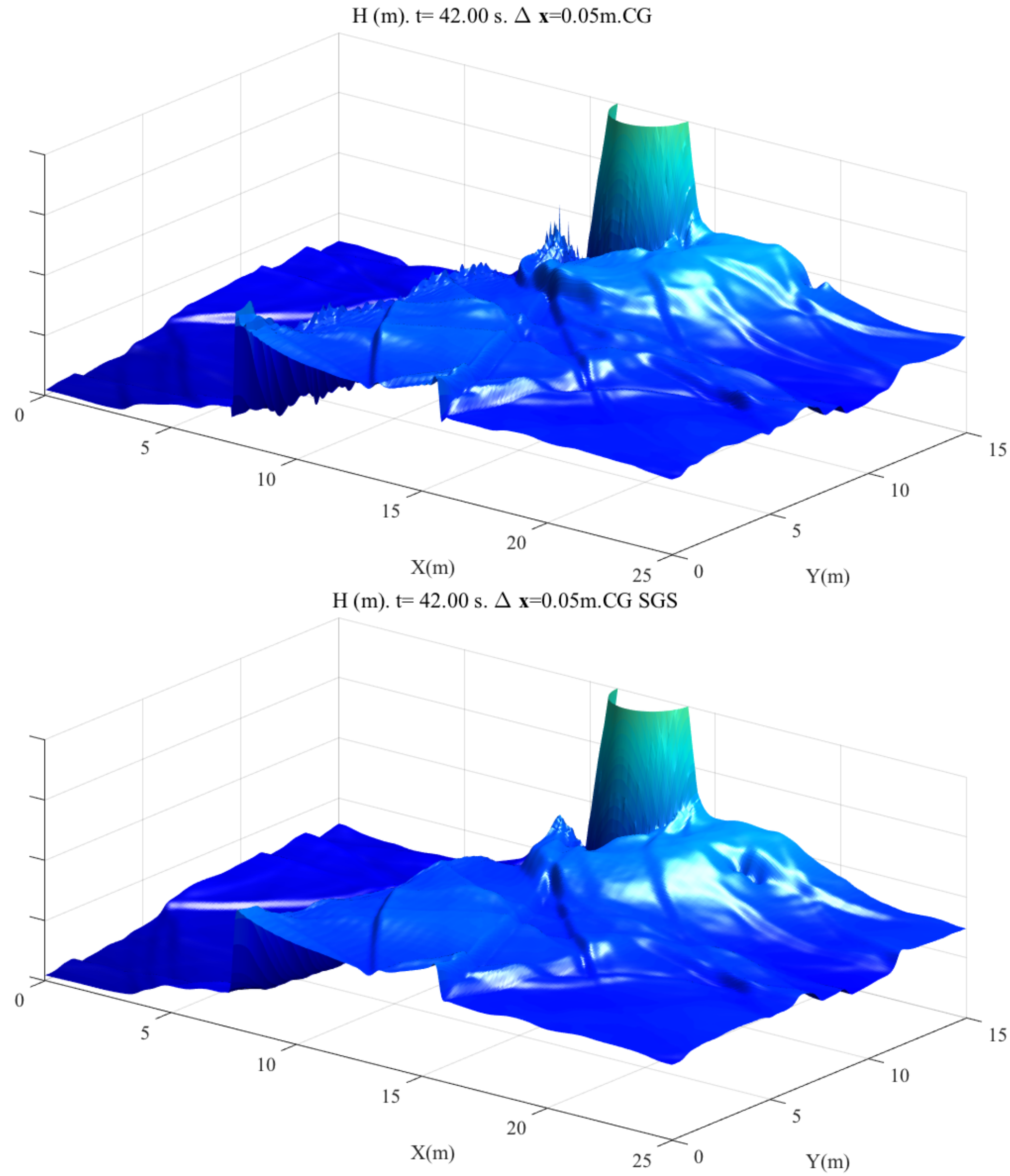

Figure 18: Like Fig. 17, but for water surface. The high frequency instabilities are removed by $Dyn-SGS$ without compromising the overall sharpness of the interacting waves. Both solutions are characterized by the same wave features at all scales.

and DG solutions at $t = 50$ s in Fig. 19. The difference between the CG and DG curves is striking. The viscous and inviscid DG spectra overlap almost fully and show approximately the same decay across the entire spectrum, from a -5/3 slope in the inertial sub-range to a -3 slope in the dissipation wave numbers (refer to [8] for a review on two-dimensional flows and their energetics). This is only true as long as the resolution is not too coarse, especially so in the case of CG. At very coarse resolutions ($\Delta\mathbf{x} \geq 0.4$ m), neither CG or DG can avoid energy from building up in the highest modes unless artificial viscosity is used. The inherent viscosity of DG is no longer sufficient to prevent this.

We stated above that μ_{SGS} is only active where the equation residuals (i.e. gradients) are important. In the case of water waves, this occurs in the proximity of the wave fronts. In Fig. 20, we plot μ_{SGS} to show its spatial structure and its evolution between $t = 0$ and $t = 50$ seconds. This plot clearly shows how viscosity is equally zero away from the fronts and only activates where really necessary. It may not be so obvious to achieve this by using an artificial viscosity that is not residual-based. To provide a visual correlation between μ_{SGS} and the wave features, in Fig. 21 we plot the stabilized spectral element solution of the water surface at a grid resolution $\Delta x \approx 0.05$ m.

7. Conclusions

We presented a shock capturing scheme, or dynamic sub-grid scale artificial viscosity that we called $Dyn - SGS$, to stabilize the high-order numerical solution of the shallow water equations via continuous and discontinuous spectral elements (CG/DG). By numerical examples, we demonstrated that this model removes the Gibbs oscillations that form in the proximity of sharp wave fronts while preserving their strength. This is possible because of the residual-based definition of the dy-

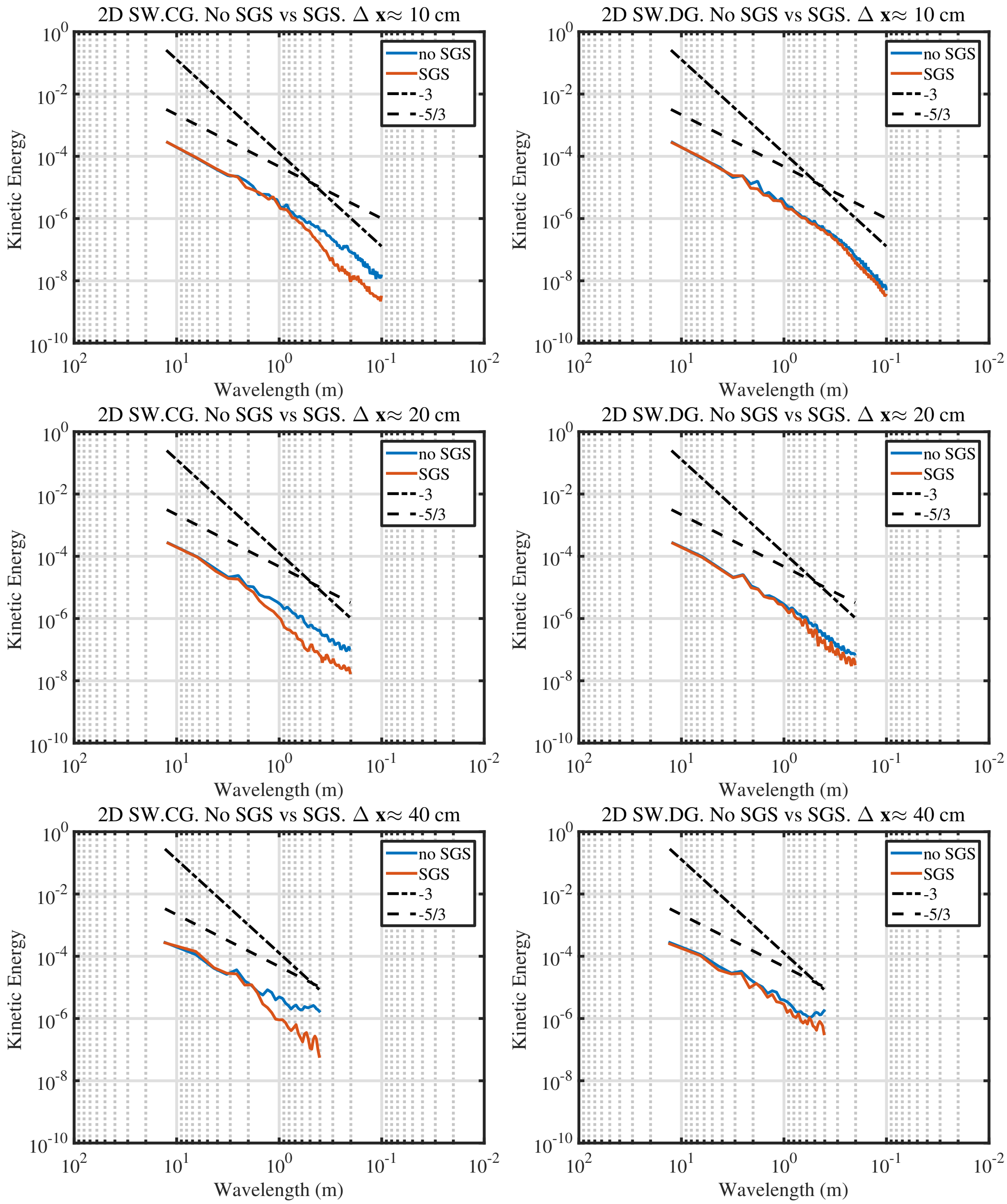

Figure 19: Instantaneous 1D energy spectra of the single hill problem of Fig. 12 at $t = 50$ s. Left: CG with and without viscosity. Right: DG with and without viscosity. From top to bottom the resolution decreases.

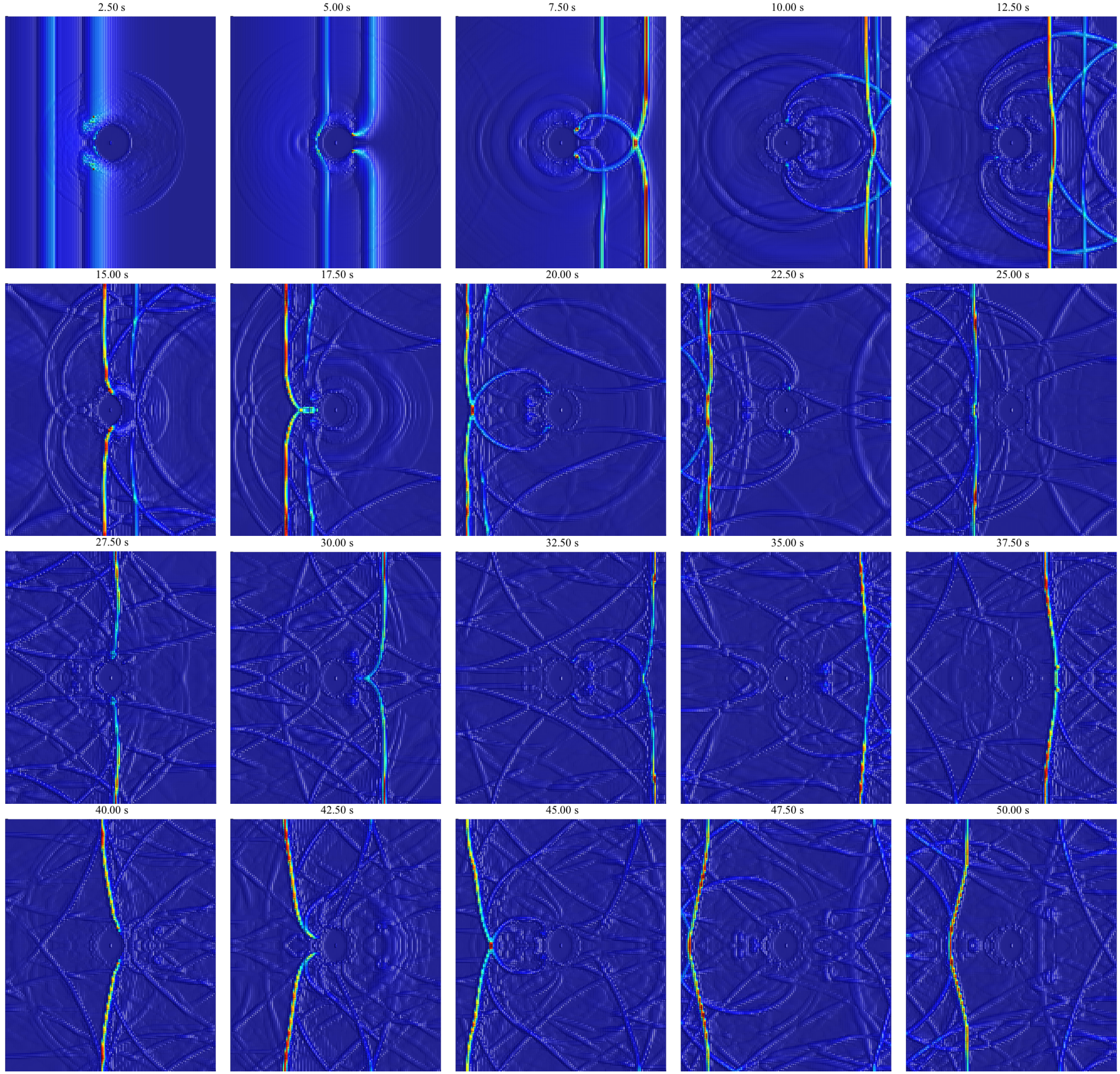

Figure 20: Time evolution of μ_{SGS} from $t = 0$ s to $t = 50$ s. The colorscale ranges between 0 (blue) and 5 (red) m^2/s. The plotted domain is $\Omega = [0, 25] \times [-15, 15]$ m^2.

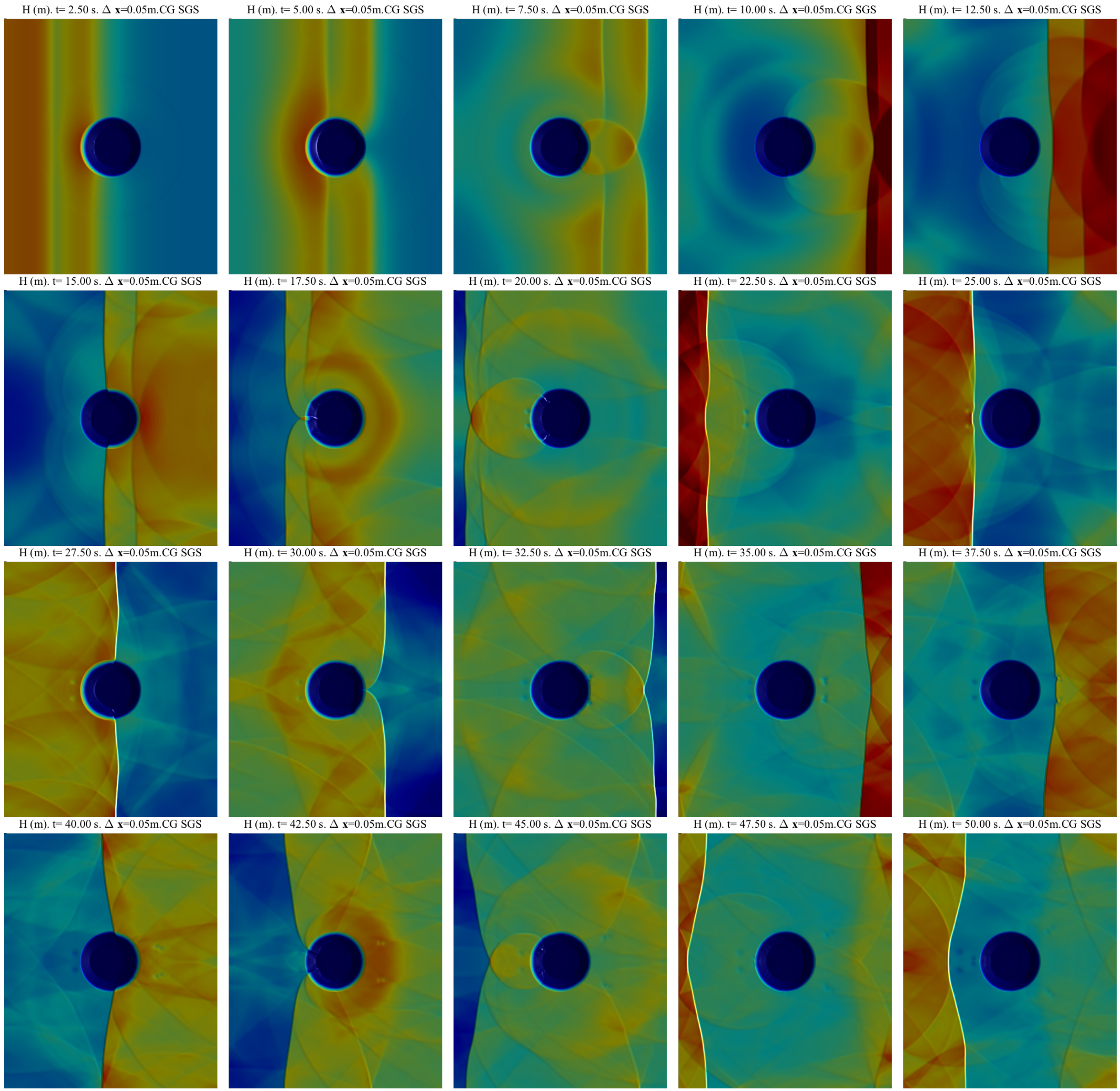

Figure 21: Time evolution of H from $t=0$ s to $t=50$ s. The color scale ranges between 0.25 (blue) and 0.5 (red) m. The plotted domain is $\Omega=[0,25]\times[-15,15]$ m^2.

namic viscosity coefficient. For coarse grids, it prevents energy from building up at small wave-numbers; this aspect is important to preserve numerical stability of tsunami simulations over large domains discretized with coarse grids. The model has no user tunable parameter, which is of great advantage when the model is to be used by an external user. When applied to the continuity equation, mass conservation is not affected. This shock capturing model works especially well for bores propagating on wet surfaces but is often not sufficient to stabilize velocity at the wet/dry interfaces, where a thin layer of water still had to be added and, in some cases, supported by additional limiting. Further work on the interaction between shock capturing, limiters, and Riemann solvers needs to be done; we did not address it in this study as it requires a thorough analysis of its own.

It is important to underline that the natural, built-in viscosity of DG may be large enough that the contribution of $Dyn-SGS$ is at times irrelevant. When this happens, the dynamic viscosity detects it from the residual, and hence limits its own strength. Nevertheless, we have shown that it is often the case that the inherent DG viscosity alone cannot prevent instabilities from forming and propagating; even if the solution does not break –as it would do in the case of CG– it still requires the support of $Dyn-SGS$. Although the results show that DG is superior to CG, we show results for both methods because many researchers use CG and it is not yet clear which method is superior in terms of robustness and efficiency (See [2] for more on these aspects.)

8. Acknowledgments

The authors would like to acknowledge the contribution of Haley Lane, who implemented the one-dimensional version of the wetting and drying algorithm used in this work. The authors would also like to acknowledge Karoline Hood who tested the correctness of the implicit solver in her NPS Master's thesis ([32]). The authors are also thankful to Prof. Fringer and Dr. Rogers for discussions regarding coastal flows, and to Stephen R. Guimond for providing his MATLAB functions to compute the energy spectra. FXG acknowledges the support of the ONR Computational Mathematics program, and FXG and EMC acknowledge the support of AFOSR Computational Mathematics.

[1] The third international workshop on long-wave runup models: Benchmark problem #1: Tsunami runup onto a plane beach. http://isec.nacse.org/workshop/2004_cornell/bmark1.html. 2004.

[2] D. Abdi, F. X. Giraldo, E. Constantinescu, L. E. Carr, L. C. Wilcox, and T. C. Warburton. Acceleration of the Implicit-Explicit Non-hydrostatic Unified Model of the Atmosphere (NUMA) on manycore processors. *Submitted. Pre-print available at https://www.researchgate.net/publication/309399443_Acceleration_of_the_Implicit-Explicit_Non-hydrostatic_Unified_Model_of_the_Atmosphere_NUMA_on_Manycore_Processors*, 2017.

[3] D. Abdi, L. C. Wilcox, T. Warburton, and F. X. Giraldo. A GPU accelerated continuous and discontinuous Galerkin non-hydrostatic atmospheric model. *Submitted. Pre-print available at www.researchgate.net/publication/290193830_A_GPU_Accelerated_Continuous_and_Discontinuous_Galerkin_Non-hydrostatic_Atmospheric_Model*, 2016.

[4] D. S. Abdi and F. X. Giraldo. Efficient construction of unified continuous and discontinuous Galerkin formulations for the 3D Euler equations. *J. Comput. Phys.*, 320:46–68, 2016.

[5] M. Ainsworth, P. Monk, and W. Muniz. Dispersive and dissipative properties of discontinuous Galerkin finite element methods for the second-order wave equation. *J. Sci. Comput.*, 27:5–40, 2006.

[6] D. Arnold. An interior penalty finite element method with discontinuous elements. *SIAM J. Numer. Anal.*, 19:742–760, 1982.

[7] N. Beisiegel and B. Behrens. Quasi-nodal third-order Bernstein polynomioals in a discontinuous Galerkin model for flooding and drying. *Environ. Earth Sci.*, 74:7275–7284, 2015.

[8] G. Boffetta and E. Ecke. Two-dimensional turbulence. *Annu. Rev. Fluid Mech.*, 44:427–451, 2012.

[9] J. P. Boyd. The erfc-log filter and the asymptotics of the Euler and Vandeven sequence accelerations. In *A.V. Ilin, L.R. Scott (Eds.), Proceedings of the Third International Conference on Spectral and High Order Methods, Houston Journal of Mathematics*, pages 267–276, 1996.

[10] M. J. Briggs, C. E. Synolakis, G. S. Harkins, and D. R. Green. Laboratory experiments of tsunami runup on a circular islad. *Pageoph.*, 144:569–593, 1995.

[11] S. Bunya, E. J. Kubatko, J. J. Westerink, and C. Dawson. A wetting and drying treatment for the Runge-Kutta discontinuous Galerkin solution to the shallow water equations. *Comput. Methods Appl. Mech. Engrg.*, 198:1548–1562, 2009.

[12] J.C. Butcher and P. Chartier. The effective order of singly-implicit Runge-Kutta methods. *Numerical Algorithms*, 20(4):269–284, 1999.

[13] G. F. Carrier, T. T. Wu, and H. Yeh. Tsunami run-up and draw-down on a plane beach. *J. Fluid Mech.*, 475:79–99, 2003.

[14] S. Chun and C. Eskilsson. Method of moving frames to solve the shallow water equations on arbitrary rotating curved surfaces. *J. Comput. Phys.*, 333:1–23, 2016.

[15] C Dawson and V. Aizinger. A discontinuous Galerkin method for three-dimensional shallow water equations. *J. Sci. Comp.*, 22:245–267, 2995.

[16] A. J. C. de Saint-Venant. Théorie du mouvement non-permanent de eaux, avec application aux crues de rivières et à l'introduction des marées dans leur lit. *C. R. Acad. Sc. Paris*, 73:147–154, 1871.

[17] O. Delestre, C. Lucas, P. A. Ksinant, F. Darboux, C. Laguerre, T. N. T. Vo, F. James, and S. Corier. SWASHES: a compilation of shallow water analytic solutions for hydraulic and environmental studies. *Int. J. Numer. Methods Fluids*, 72:269–300, 2013.

[18] C. Eskilsson. An hp/adaptive discontinuous Galerkin method for shallow water flows. *Int. J. Numer. Methods Fluids*, 67:1605–1623, 2011.

[19] J. M. Gallardo, C. Parés, and M. Castro. On a well-balanced high-order finite volume scheme for shallow water equations with topography and dry areas. *J. Comput. Phys.*, 227:574–601, 2007.

[20] R. Gandham, D. Medina, and T. Warburton. GPU accelerated discontinuous galerkin methods for shallow water equations. *Commun. Comput. Phys.*, 18:37–64, 2015.

[21] J. F. Gerbeau and B. Perthame. Derivation of the viscous Saint-Venant system for laminar shallow water; numerical validation. *Discrete Contin. Dyn. Syst. Ser. B*, 1:89–102, 2001.

[22] N. Gerhard, D. Caviedes-Voulième, S. Müller, and G. Kesserwani. Multiwavelet-based grid adaptation with discontinuous Galerkin schemes for shallow water equations. *J. Comput. Phys.*, 301:265–288, 2015.

[23] F. X. Giraldo. A spectral element shallow water model on spherical geodesic grids. *Int. J. Num. Meth. Fluids*, 35:869–901, 2001.

[24] F. X. Giraldo, J. S. Hesthaven, and T. Warburton. Nodal high-order discontinuous Galerkin methods for spherical shallow water equations. *J. Comput. Phys.*, 181:499–525, 2002.

[25] F X. Giraldo, J F.. Kelly, and E. Constantinescu. Implicit-explicit formulations of a three-dimensional Nonhydrostatic Unified Model of the Atmosphere (NUMA). *SIAM J. Sci. Comput.*, 35:1162–1194, 2013.

[26] F. X. Giraldo and M. Restelli. High-order semi-implicit time-integrators for a triangular discontinuous Galerkin oceanic shallow water model. *Int. J. Numer. Methods Fluids*, 63:1077–1102, 2010.

[27] S. Gottlieb, C.-W. Shu, and E. Tadmor. Strong stability-preserving high-order time discretization methods. *SIAM review*, 43(1):89–112, 2001.

[28] R. Gourgue, O. Comblen, J. Lambrechts, T. Kärnä, V. Legat, and E. Deleersnijder. A flux-limiting wetting-drying method for finite-element shallow-water models, with application to the Scheldt Estuary. *Adv. Water Resourc.*, 32:1726–1739, 2009.

[29] O. Guba, M. A. Taylor, P. A. Ullrich, J. R. Overfelt, and M. N. Levy. The spectral element method on variable resolution grids: evaluating grid sensitivity and resolution-aware numerical viscosity. *Geosci. Model Dev. Discuss.*, 7:4081–4117, 2014.

[30] J L. Guermond and B. Popov. Viscous regularization of the Euler equations and entropy principles. *SIAM J. Appl. Math.*, 74(2):284–305, 2014.

[31] E. Hendricks, M. Kopera, and F. X. Giraldo. Evaluation of the utility of static and adaptive mesh refinement for idealized tropical cyclone problems in a spectral element shallow water model. *Mon. Wea. Rev. (in press)*, 2016.

[32] K. Hood. Modeling storm surge using discontinuous Galerkin methods. *Masters Thesis, Dept. of Applied Maths, Naval Postgraduate School, Monterey, CA, U.S.A.*, 2016.

[33] M. Iskandarani, D .B. Haidvogel, and J. P. Boyd. A staggered spectral element models with application to the oceanic shallow water equations. *Int. J. Numer. Methods Fluids*, 20:393–414, 1995.

[34] T. Kärnä, B. de Brye, O. Gourgue, J. Lambrechts, R. Comblen, V. Legat, and E. Deleersnijder. A fully implicit wetting-drying method for DG-FEM shallow water models, with an application to the Scheldt Estuary. *Comp. Methods Appl. Mech. Engrg.*, 200:509–524, 2011.

[35] C.A. Kennedy and M.H. Carpenter. Additive Runge-Kutta schemes for convection-diffusion-reaction equations. *Appl. Numer. Math.*, 44(1-2):139–181, 2003.

[36] G. Kesserwani and Q. Liang. A conservative high-order discontinuous Galerkin method for the shallow water equations with arbitrary topography. *Numer. Methods Eng.*, 86:47–69, 2011.

[37] G. Kesserwani and Q. Liang. Dynamically adaptive grid based discontinuous Galerkin shallow water model. *Adv. Water Res.*, 37:23–39, 2012.

[38] G. Kesserwani and Q. Liang. Locally limited and fully conserved RKDG2 shallow water solutions with wetting and drying. *J. Sci. Comp.*, 50:120–144, 2012.

[39] D.A. Knoll and D.E. Keyes. Jacobian-free Newton–Krylov methods: a survey of approaches and applications. *Journal of Computational Physics*, 193(2):357–397, 2004.

[40] M. A. Kopera and F. X. Giraldo. Analysis of adaptive mesh refinement for IMEX discontinuous Galerkin solutions of the compressible Euler equations with application to atmospheric simulations. *J. Comput. Phys.*, 92-117:275, 2014.

[41] M. A. Kopera and F. X. Giraldo. Mass conservation of the unified continuous and discontinuous element-based galerkin methods on dynamically adaptive grids with application to atmospheric simulations. *J. Comput. Phys.*, 297:90–103, 2015.

[42] E. J. Kubatko, J. J. Westerink, and C. Dawson. *hp* discontinuous Galerkin methods for advection dominated problems in shallow water flow. *Comp. Methods Appl. Mech. Engrg.*, 196:437–451, 2006.

[43] R. LeVeque. *Finite volume methods for hyperbolic problems*. Cambridge University Press, 1st edition, 2002.

[44] M. Li, P. Guyenne, F. Li, and L. Xi. A positivity-preserving well-balanced central discontinuous Galerkin method for the nonlinear shallow water equations. *J. Sci. Comput. (in press)*, 2016.

[45] D. K. Lilly. On the numerical simulation of buoyant convection. *Tellus*, 14:148–172, 1962.

[46] H. Ma. A spectral element basin model for the shallow water equations. *J. Comput. Phys.*, 109:133–149, 1993.

[47] S. Marras, M. A. Kopera, and F X. Giraldo. Simulation of shallow water jets with a unified element-based continuous/discontinuous Galerkin model with grid flexibility on the sphere. *Q. J. Roy. Meteor. Soc.*, 141:1727–1739, 2015.

[48] S. Marras, M. Nazarov, and F. X. Giraldo. Stabilized high-order Galerkin methods based on a parameter-free dynamic SGS model for LES. *J. Comput. Phys.*, 301:77–101, 2015.

[49] C. Michoski, C. Dawson, E. J. Kubatko, D. Wirasaet, S. Brus, and J. J. Westerink. A comparison of artificial viscosity, limiters, and filters, for high order discontinuous Galerkin solutions in nonlinear settings. *J. Sci. Comput.*, 66:406–434, 2016.

[50] A. Müller, M. A. Kopera, S. Marras, L .C. Wilcox, T. Isaac, and F. X. Giraldo. Strong Scaling for Numerical Weather Prediction at Petascale with the Atmospheric Model NUMA. *Submitted to the IEEE International Parallel and Distributed Processing Symposium. Pre-print available at www.researchgate.net/publication282887372_Strong_Scaling_for_Numerical_Weather_Prediction_at_Petascale_with_the_Atmospheric_Model_NUMA*, 2016.

[51] R D. Nair, S J. Thomas, and R D. Loft. A discontinuous Galerkin global shallow water model. *Mon. Wea. Rev.*, 133, 2007.

[52] M. Nazarov and J. Hoffman. Residual-based artificial viscosity for simulation of turbulent compressible flow using adaptive finite element methods. *Int. J. Numer. Methods Fluids*, 71:339–357, 2013.

[53] R. Pasquetti, J.L. Guermond, and B. Popov. Stabilized spectral element approximation of the Saint Venant system using the entropy viscosity technique. In *Spectral and High Order Methods for Partial Differential Equations ICOSAHOM 2014, Lecture Notes in Computational Science and Engineering*, pages 397–404, 2015.

[54] C. Phan Van, E. Deleersnijder, D. Bousmar, and S. Frazão Soares. Simulation of flow in compound open-channel using a discontinuous Galerkin finite-element method with Smagorinsky turbulence closure. *J. Hydro-env. Research*, 8:396–409, 2014.

[55] N. Rakowsky, A. Androsov, A. Fuchs, S. Harig, A. Immerz, S. Danilov, W. Hiller, and J. Schröter. Operational tsunami modelling with TsunAWI - recent developments and applications. *Nat. Haz. Earth Sys. Sci.*, 13:1629–1642, 2013.

[56] J. Smagorinsky. General circulation experiments with the primitive equations: I. the basic experiement. *Mon. Wea. Rev.*, 91:99–164, 1963.

[57] J .J. Stoker. *Water Waves: The Mathematical Theory with Applications*, volume 4. John Wiley and Sons, 1957.

[58] C. E. Synolakis. The runup of solitary waves. *J. Fluid Mech.*, 185:523–545, 1987.

[59] M. Taylor, J. Tribbia, and M. Iskandarani. The spectral element method for the shallow water equations on the sphere. *J. Comput. Phys.*, 130:92–108, 1997.

[60] W. C. Thacker. Some exact solutions to the nonlinear shallow-water wave equations. *J. Fluid Mech.*, 107:499–508, 1981.

[61] E. Toro. *Shock-capturing methods for free-surface shallow flows.* Wiley, 2nd edition, 2001.

[62] G. Tumolo and L. Bonaventura. A semi-implicit, semi-Lagrangian discontinuous Galerkin framework for adaptive numerical weather prediction: SISL-DG Framework for Adaptive NWP. *Q. J. Roy. Meteor. Soc.*, 141:692–, 2015.

[63] H. Vandeven. Family of spectral filters for discontinuous problems. *J. Sci. Comp.*, 6:159–192, 1991.

[64] S. Vater, N. Beisiegel, and J. Behrens. A limiter-based well-balanced discontinuous Galerkin method for shallow-water flows with wetting and drying: one dimensional case. *Adv. Water Res.*, 85:1–13, 2015.

[65] Y. Xing, X. Zhang, and C. W. Shu. Positivity-preserving high order well-balanced discontinuous Galerkin methods for the shallow water equations. *Adv. Water Res.*, 33:1476–1493, 2010.